The Astrophysical Journal, 799:137 (14pp), 2015 February 1 doi:10.1088/0004-637X/799/2/137

MEASUREMENT OF GALAXY CLUSTER INTEGRATED COMPTONIZATION AND MASS SCALING RELATIONS WITH THE SOUTH POLE TELESCOPE

B. R. Saliwanchik[1], T. E. Montroy[1], K. A. Aird[2], M. Bayliss[3,4], B. A. Benson[5,6,7], L. E. Bleem[5,8,9], S. Bocquet[10,11], M. Brodwin[12], J. E. Carlstrom[5,6,8,9,13], C. L. Chang[5,6,9], H. M. Cho[14], A. Clocchiatti[15], T. M. Crawford[5,13], A. T. Crites[5,13], T. de Haan[16], S. Desai[10,11], M. A. Dobbs[16], J. P. Dudley[16], R. J. Foley[4,17,18], W. R. Forman[4], E. M. George[19], M. D. Gladders[5,13], A. H. Gonzalez[20], N. W. Halverson[21], J. Hlavacek-Larrondo[22,23], G. P. Holder[16], W. L. Holzapfel[19], J. D. Hrubes[2], C. Jones[4], R. Keisler[5,8], L. Knox[24], A. T. Lee[19,25], E. M. Leitch[5,13], J. Liu[10,11], M. Lueker[19,26], D. Luong-Van[2], A. Mantz[5], D. P. Marrone[27], M. McDonald[28], J. J. McMahon[29], J. Mehl[5,13], S. S. Meyer[5,6,8,13], L. Mocanu[5,13], J. J. Mohr[10,11,30], S. S. Murray[4], D. Nurgaliev[3], S. Padin[5,13,26], A. Patej[3], C. Pryke[31], C. L. Reichardt[19], A. Rest[32], J. Ruel[3], J. E. Ruhl[1], A. Saro[10], J. T. Sayre[1], K. K. Schaffer[5,6,33], E. Shirokoff[19,26], H. G. Spieler[25], B. Stalder[4], S. A. Stanford[24,34], Z. Staniszewski[1], A. A. Stark[4], K. Story[5,8], C. W. Stubbs[3,4], K. Vanderlinde[35,36], J. D. Vieira[17,26], A. Vikhlinin[4], R. Williamson[5,13], O. Zahn[19,25,37], and A. Zenteno[11]

[1] Physics Department, Center for Education and Research in Cosmology and Astrophysics, Case Western Reserve University, Cleveland, OH 44106, USA; benjamin.saliwanchik@case.edu
[2] University of Chicago, 5640 South Ellis Avenue, Chicago, IL 60637, USA
[3] Department of Physics, Harvard University, 17 Oxford Street, Cambridge, MA 02138, USA
[4] Harvard-Smithsonian Center for Astrophysics, 60 Garden Street, Cambridge, MA 02138, USA
[5] Kavli Institute for Cosmological Physics, University of Chicago, 5640 South Ellis Avenue, Chicago, IL 60637, USA
[6] Enrico Fermi Institute, University of Chicago, 5640 South Ellis Avenue, Chicago, IL 60637, USA
[7] Center for Particle Astrophysics, Fermi National Accelerator Laboratory, Batavia, IL 60510, USA
[8] Department of Physics, University of Chicago, 5640 South Ellis Avenue, Chicago, IL 60637, USA
[9] Argonne National Laboratory, 9700 S. Cass Avenue, Argonne, IL 60439, USA
[10] Department of Physics, Ludwig-Maximilians-Universität, Scheinerstr. 1, D-81679 München, Germany
[11] Excellence Cluster Universe, Boltzmannstr. 2, D-85748 Garching, Germany
[12] Department of Physics and Astronomy, University of Missouri, 5110 Rockhill Road, Kansas City, MO 64110, USA
[13] Department of Astronomy and Astrophysics, University of Chicago, 5640 South Ellis Avenue, Chicago, IL 60637, USA
[14] NIST Quantum Devices Group, 325 Broadway, Mailcode 817.03, Boulder, CO 80305, USA
[15] Departamento de Astronomia y Astrofisica, Pontificia Universidad Catolica, Chile
[16] Department of Physics, McGill University, 3600 Rue University, Montreal, QC H3A 2T8, Canada
[17] Astronomy Department, University of Illinois at Urbana-Champaign, 1002 W. Green Street, Urbana, IL 61801, USA
[18] Department of Physics, University of Illinois at Urbana-Champaign, 1110 W. Green Street, Urbana, IL 61801, USA
[19] Department of Physics, University of California, Berkeley, CA 94720, USA
[20] Department of Astronomy, University of Florida, Gainesville, FL 32611, USA
[21] Department of Astrophysical and Planetary Sciences and Department of Physics, University of Colorado, Boulder, CO 80309, USA
[22] Kavli Institute for Particle Astrophysics and Cosmology, Stanford University, 452 Lomita Mall, Stanford, CA 94305, USA
[23] Department of Physics, Stanford University, 452 Lomita Mall, Stanford, CA 94305, USA
[24] Department of Physics, University of California, One Shields Avenue, Davis, CA 95616, USA
[25] Physics Division, Lawrence Berkeley National Laboratory, Berkeley, CA 94720, USA
[26] California Institute of Technology, 1200 E. California Boulevard, Pasadena, CA 91125, USA
[27] Steward Observatory, University of Arizona, 933 North Cherry Avenue, Tucson, AZ 85721, USA
[28] Kavli Institute for Astrophysics and Space Research, Massachusetts Institute of Technology, 77 Massachusetts Avenue, Cambridge, MA 02139, USA
[29] Department of Physics, University of Michigan, 450 Church Street, Ann Arbor, MI 48109, USA
[30] Max-Planck-Institut für extraterrestrische Physik, Giessenbachstrasse, D-85748 Garching, Germany
[31] Physics Department, University of Minnesota, 116 Church Street S.E., Minneapolis, MN 55455, USA
[32] Space Telescope Science Institute, 3700 San Martin Drive, Baltimore, MD 21218, USA
[33] Liberal Arts Department, School of the Art Institute of Chicago, 112 S Michigan Avenue, Chicago, IL 60603, USA
[34] Institute of Geophysics and Planetary Physics, Lawrence Livermore National Laboratory, Livermore, CA 94551, USA
[35] Dunlap Institute for Astronomy & Astrophysics, University of Toronto, 50 St. George Street, Toronto, ON M5S 3H4, Canada
[36] Department of Astronomy & Astrophysics, University of Toronto, 50 St. George Street, Toronto, ON M5S 3H4, Canada
[37] Berkeley Center for Cosmological Physics, University of California, Berkeley, CA 94720, USA

Received 2013 December 10; accepted 2014 November 20; published 2015 January 22

ABSTRACT

We describe a method for measuring the integrated Comptonization (Y_{SZ}) of clusters of galaxies from measurements of the Sunyaev–Zel'dovich (SZ) effect in multiple frequency bands and use this method to characterize a sample of galaxy clusters detected in the South Pole Telescope (SPT) data. We use a Markov Chain Monte Carlo method to fit a β-model source profile and integrate Y_{SZ} within an angular aperture on the sky. In simulated observations of an SPT-like survey that include cosmic microwave background anisotropy, point sources, and atmospheric and instrumental noise at typical SPT-SZ survey levels, we show that we can accurately recover β-model parameters for inputted clusters. We measure Y_{SZ} for simulated semi-analytic clusters and find that Y_{SZ} is most accurately determined in an angular aperture comparable to the SPT beam size. We demonstrate the utility of this method to measure Y_{SZ} and to constrain mass scaling relations using X-ray mass estimates for a sample of 18 galaxy clusters from the SPT-SZ survey. Measuring Y_{SZ} within a 0.′75 radius aperture, we find an intrinsic log-normal scatter of 21% ± 11% in Y_{SZ} at a fixed mass. Measuring Y_{SZ} within a 0.3 Mpc projected radius (equivalent to 0.′75 at the survey median redshift $z = 0.6$), we find a scatter of 26% ± 9%. Prior to this study, the SPT observable found to

have the lowest scatter with mass was cluster detection significance. We demonstrate, from both simulations and SPT observed clusters that Y_{SZ} measured within an aperture comparable to the SPT beam size is equivalent, in terms of scatter with cluster mass, to SPT cluster detection significance.

Key words: galaxies: clusters: general – methods: data analysis – X-rays: galaxies: clusters

1. INTRODUCTION

Galaxy clusters are the largest gravitationally collapsed systems in the observed universe, and their abundance as a function of mass and redshift is a sensitive probe of the growth of structure in the universe. The ability to accurately and precisely estimate cluster masses is essential for using them to constrain cosmological parameters. Typically this is done through cluster observables, which do not directly measure cluster mass, but can be related to it through scaling relations (Vikhlinin et al. 2009b; Rozo et al. 2010; Mantz et al. 2010; Benson et al. 2013). The Sunyaev–Zel'dovich (SZ) effect (Sunyaev & Zel'dovich 1972) is caused by the inverse Compton scattering of cosmic microwave background (CMB) photons off of hot intra-cluster gas. It is a measure of the line-of-sight integral of the cluster pressure and is expected to be a low scatter proxy for cluster mass (Carlstrom et al. 2002; Kravtsov et al. 2006). In particular, the integrated Comptonization of a cluster, Y_{SZ}, is expected to have a low intrinsic scatter with cluster mass and to be relatively insensitive to cluster astrophysics (Barbosa et al. 1996; Holder & Carlstrom 2001; Motl et al. 2005; Nagai et al. 2007; Fabjan et al. 2011).

However, for SZ observations where the cluster size is on the order of the instrument beam size or smaller, there is typically a degeneracy in the constraints on the amplitude and shape of the assumed cluster profile (e.g., Benson et al. 2004; Planck Collaboration et al. 2011a, 2013a). One potential way of handling this degeneracy is to employ a Bayesian or Monte Carlo analysis method. A number of experiments have used Monte Carlo methods to characterize the profiles of galaxy clusters in recent years, including Bolocam (Sayers et al. 2013), the Arcminute Microkelvin Imager (AMI; AMI Consortium et al. 2012a, 2012b), the Planck Collaboration (Planck Collaboration et al. 2012; Planck and AMI Collaborations et al. 2013), and the Atacama Cosmology Telescope (ACT) and Sunyaev–Zel'dovich Array (SZA; Reese et al. 2012). In this work, we present a Markov Chain Monte Carlo (MCMC) analysis method for analyzing observations of the SZ effect, which measures Y_{SZ} while marginalizing other SZ model parameters. A feature of the MCMC method is that the Y_{SZ} estimates it produces are well constrained even for clusters with relatively small radii on the sky. This method is related to the method presented in T. E. Montroy et al. (2015, in preparation), which uses the same likelihood, but employs a rapid grid method to directly evaluate the likelihood throughout the parameter space.

We apply this MCMC method to simulated and real observations from the South Pole Telescope (SPT). Various experiments have examined scaling relations between SZ signal and optical or X-ray data. The Planck Collaboration has examined Y_{SZ}–L_X scaling relations (Planck Collaboration et al. 2011b) and Y_{SZ}–M_X scaling relations (Planck Collaboration et al. 2013b). Sehgal et al. (2011), Sifon et al. (2013), and Hasselfield et al. (2013) investigate the scaling between central Comptonization, y_0, or Y_{SZ} and mass for ACT clusters. Previous analyses of clusters observed in the SPT-SZ survey used the cluster detection significance, ξ, as a proxy for cluster mass (Vanderlinde et al. 2010; Andersson et al. 2011; Benson et al. 2013; Reichardt et al. 2013). Here we show that Y_{SZ} integrated over a fixed angular aperture near the SPT beam size and ξ have comparable fractional scatter in their respective mass scaling relations. Y_{SZ}, however, is more easily compared to cluster parameters derived from other measurements.

2. CLUSTER SAMPLE AND OBSERVATIONS

2.1. SZ Observations

The SPT is a 10 m diameter off-axis Gregorian telescope with a 1 deg^2 field of view, designed to operate at millimeter and submillimeter wavelengths (Carlstrom et al. 2011). In 2007–2011, the SPT surveyed 2500 deg^2 in three frequency bands centered at 95, 150, and 220 GHz. This survey is referred to as the SPT-SZ survey. The cluster sample used in this work is drawn from the two fields ($\sim$100 deg^2 each) observed with the SPT in 2008, one centered at right ascension (R.A.) 5^h30^m, declination (decl.) -55° (J2000), and one at R.A. 23^h30^m, decl. -55°. A nearly identical cluster sample was used in Vanderlinde et al. (2010, hereafter V10), Andersson et al. (2011, hereafter A11), and Benson et al. (2013, hereafter B13).

Observing procedures, data processing, and detection algorithms for these clusters are described in detail in V10 and Staniszewski et al. (2009) and are summarized here. Details of the data processing pipeline are also described in Schaffer et al. (2011).

Each field was observed by scanning the telescope back and forth in azimuth at $0.^\circ25\,s^{-1}$, and then stepping in elevation and repeating until the entire field was covered. This process covers a 100 deg^2 field in approximately two hours Field scans were repeated several hundred times until the noise in the co-added maps reached a completion depth of 18 μKarcmin for 150 GHz. (See Staniszewski et al. 2009, V10, or Williamson et al. 2011 for a description of field depth measurements.) The timestreams of the individual detectors were filtered to remove sky signal that was spatially correlated across the focal plane and long timescale detector drift. The combination of these filters effectively removes signals with angular scales larger than $\sim0.^\circ5$. Data from individual detectors were combined using inverse-variance weighting, and the resulting maps were calibrated by comparison to the *Wilkinson Microwave Anisotropy Probe* (*WMAP*) 5 yr CMB temperature anisotropy power spectrum (Lueker et al. 2010).

2.2. Cluster Detection

Clusters are identified in the SPT maps using a matched filter (MF; Haehnelt & Tegmark 1996; Herranz et al. 2002a, 2002b; Melin et al. 2006). Specifics on this procedure can be found in Staniszewski et al. (2009) and V10 for single frequency cluster detection, and in Williamson et al. (2011) and Reichardt et al. (2013) for multi-frequency detection. To locate clusters, the maps are multiplied in Fourier space with a filter matched to the expected spatial signal-to-noise (S/N) profile of galaxy clusters. The MF, ψ, is given by

$$\psi(k_x, k_y) = \frac{B(k_x, k_y)S(|\boldsymbol{k}|)}{B(k_x, k_y)^2 N_{\rm astro}(|\boldsymbol{k}|) + N_{\rm terr}(k_x, k_y)}, \quad (1)$$

where B is the instrument response after timestream filtering, S is the source template, and the noise has been divided into astrophysical ($N_{\rm astro}$) and terrestrial ($N_{\rm terr}$) components. $N_{\rm astro}$ includes power from lensed primary CMB anisotropies, an SZ background from faint undetected clusters, and millimeter-wave emitting point sources. The noise power spectrum $N_{\rm terr}$ includes atmospheric and instrumental noise, estimated from jackknife maps. The source template is a two-dimensional projection of an isothermal β-model, with β set to 1 (Cavaliere & Fusco-Femiano 1976):

$$\Delta T = \Delta T_0 \left(1 + \theta^2 / \theta_{\rm c}^2\right)^{-1}, \quad (2)$$

where the central SZ temperature decrement ΔT_0 and the core radius $\theta_{\rm c}$ are free parameters.

Clusters are detected using a (negative) peak detection algorithm similar to SExtractor (Bertin & Arnouts 1996). The significance of a detection, ξ, is defined to be the highest S/N ratio across all $\theta_{\rm c}$. In our analysis, we use the unbiased significance $\zeta = \sqrt{\langle \xi \rangle^2 - 3}$, where $\langle \xi \rangle$ is the average detection significance of a cluster across many noise realizations (V10).

It is important to note here that maximizing the S/N in the MF maximizes the likelihood used in the MCMC method below (Section 3) at a fixed $\theta_{\rm c}$. The two methods are exploring the same likelihood, the difference is that the MF is optimized for detecting clusters not parameterizing them, since it does not simultaneously explore all dimensions in the parameter space.

2.3. Optical and X-Ray Observations

The optical and X-ray observations for the clusters used in this work have previously been described in A11 and B13, which we briefly describe here. All 18 clusters have redshift measurements, 15 of which are spectroscopic, and 14 of the clusters have X-ray measurements.

Optical *griz* imaging and photometric redshifts for these clusters were obtained from the Blanco Cosmology Survey (Desai et al. 2012), and from pointed observations using the Magellan telescopes (High et al. 2010). Of the 15 clusters with spectroscopic redshifts, 8 were obtained by the Low Dispersion Survey Spectrograph (LDSS3) on the Magellan Clay 6.5 m telescope (High et al. 2010), and 1 by the Inamori Magellan Areal Camera and Spectrograph (IMACS) on the Magellan Baade 6.5 m telescope (Brodwin et al. 2010). The final six cluster redshifts were measured with IMACS and GMOS on Gemini South (Ruel et al. 2013). X-ray follow-up observations were performed with *Chandra* ACIS-I and *XMM-Newton* EPIC (A11; B13).

3. MCMC ANALYSIS METHODS

In this work, we follow a Bayesian approach to parameter estimation, using a MCMC method to estimate the parameters of our cluster source model. The application of MCMC methods to the detection and characterization of compact astrophysical sources in noisy backgrounds was proposed by Hobson & McLachlan (2003), and several experiments have used MCMC methods for parameterizing SZ signals from galaxy clusters. Bonamente et al. (2004), Bonamente et al. (2006), and LaRoque et al. (2006) used MCMC methods to analyze SZ data from BIMA and OVRO, in conjunction with X-ray data from *Chandra*, and fit β-model profiles to galaxy clusters. Muchovej et al. (2007), Culverhouse et al. (2010), and Marrone et al. (2009) parameterized SZA clusters, and Halverson et al. (2009) parameterized the Bullet Cluster using APEX-SZ data, all using the β-model. Culverhouse et al. (2010), Marrone et al. (2009), and Marrone et al. (2012) additionally estimated cluster $Y_{\rm SZ}$ values. In recent years there has been a surge of interest in MCMC methods for parameterizing cluster from a number of experiments, including Bolocam (Sayers et al. 2013), AMI (AMI Consortium et al. 2012a, 2012b), the Planck Collaboration (Planck Collaboration et al. 2012; Planck and AMI Collaborations et al. 2013), and ACT and SZA (Reese et al. 2012). Here we estimate galaxy cluster $Y_{\rm SZ}$ values and $Y_{\rm SZ}$–M scaling relations in addition to estimating β-model parameters.

3.1. Posterior Distribution for a Compact Source

We use a Metropolis–Hastings algorithm implementation of the MCMC method for parameter estimation (Metropolis et al. 1953; Hastings 1970). For the case of a compact object with source template $S(\mathcal{H})$ in a two-dimensional astronomical data set D with Gaussian noise, the Bayesian likelihood has the form

$$\mathrm{P}(D|\mathcal{H}) = \frac{\exp\left(-\frac{1}{2}[D - S(\mathcal{H})]C^{-1}[D - S(\mathcal{H})]^*\right)}{(2\pi)^{N_{\rm pix}/2}|C|^{1/2}}, \quad (3)$$

where C is the noise covariance matrix for the data set D, and $N_{\rm pix}$ is the number of pixels in D (Hobson & McLachlan 2003). In this method, C is composed of the combined $N_{\rm astro}$ and $N_{\rm terr}$ noise terms in the MF ψ (Equation (1)).

We are interested in parameterizing galaxy clusters using the SZ effect, which is the spectral distortion they produce in the blackbody CMB spectrum. At two of the SPT's observing frequencies (95 and 150 GHz), this distortion is manifested as a decrement in CMB power, while the net change in CMB power at 220 GHz is negligible.

Equation (3) is easily generalizable to the case of astronomical images in multiple frequency bands, where the unnormalized log likelihood may be calculated in the Fourier domain as

$$\log(\overline{\mathrm{P}}(D|\mathcal{H})) = -\frac{1}{2}\sum_{\bar{k},\nu_i,\nu_j}\left[\widetilde{D}_{\nu_i}(\bar{k}) - \widetilde{s}^{\mathcal{H}}_{\nu_i}(\bar{k})\right]N^{-1}_{\nu_i\nu_j}(\bar{k})\left[\widetilde{D}_{\nu_j}(\bar{k}) - \widetilde{s}^{\mathcal{H}}_{\nu_j}(\bar{k})\right]^*, \quad (4)$$

where $\bar{k}$ is the two-dimensional Fourier space vector, $\widetilde{D}_{\nu_i}(\bar{k})$ is the Fourier transform of the map for frequency ν_i, $\widetilde{s}^{\mathcal{H}}_{\nu_i}(\bar{k})$ is the frequency-dependent Fourier transform of the cluster model for parameter set $\mathcal{H}$, and $N_{\nu_i\nu_j}(\bar{k})$ is the frequency-dependent covariance matrix for the ν_i and ν_j frequency maps. Here $N_{\nu_i\nu_j}(\bar{k})$ is simply the multiband extension of the covariance matrix C in Equation (3). It is convenient to perform the likelihood calculations in Fourier space rather than physical space because $N_{\nu_i\nu_j}(\bar{k})$ is diagonal in Fourier space, assuming stationary noise.

The frequency-dependent covariance matrix is computed as follows. For a given $\bar{k}$, the two frequency matrix for CMB+Noise covariance is

$$N_{\nu_i\nu_j}(\bar{k}) = \begin{bmatrix} C(\bar{k})B_1(\bar{k})^2 + N_1(\bar{k}) & C(\bar{k})B_1(\bar{k})B_2(\bar{k}) \\ C(\bar{k})B_1(\bar{k})B_2(\bar{k}) & C(\bar{k})B_2(\bar{k})^2 + N_2(\bar{k}) \end{bmatrix} \quad (5)$$

where $C(\bar{k})$ is the CMB power at $\bar{k}$, $B_1(\bar{k})$ and $N_1(\bar{k})$ are the beam and noise for the first frequency, and $B_2(\bar{k})$ and $N_2(\bar{k})$ are the beam and noise for the second frequency.

The covariance becomes more complicated when including point sources and the SZ background because the signal component has a different magnitude at different frequencies. If $Q_1(\bar{k})$ and $Q_2(\bar{k})$ are the point source or SZ covariance at two of our observing frequencies, then we have

$$N_{\nu_i\nu_j}(\bar{k}) = \begin{bmatrix} C(\bar{k})B_1(\bar{k})^2 + N_1(\bar{k}) + B_1(\bar{k})^2 Q_1(\bar{k}) & \\ \quad C(\bar{k})B_1(\bar{k})B_2(\bar{k}) + B_1(\bar{k})B_2(\bar{k})\sqrt{Q_1(\bar{k})Q_2(\bar{k})} & \\ C(\bar{k})B_1(\bar{k})B_2(\bar{k}) + B_1(\bar{k})B_2(\bar{k})\sqrt{Q_1(\bar{k})Q_2(\bar{k})} & \\ \quad C(\bar{k})B_2(\bar{k})^2 + N_2(\bar{k}) + B_2(\bar{k})^2 Q_2(\bar{k}) & \end{bmatrix}. \quad (6)$$

Before the log-likelihood is calculated, to account for the filtering of the data set $\widetilde{D}_{\nu_i}(\bar{k})$ as described in Section 2.1, both the covariance $N_{\nu_i\nu_j}(\bar{k})$, and the source template $\widetilde{s}^{\mathcal{H}}_{\nu_i}(\bar{k})$, are multiplied by a Fourier space filter function that emulates the timestream filtering used to produce $\widetilde{D}_{\nu_i}(\bar{k})$.

3.2. Implementation

Our MCMC is modeled after the generic Metropolis–Hastings method described in Hobson & McLachlan (2003), and is implemented in MATLAB[38].

In this work, we use the MCMC method for cluster parameterization, not detection. Our testing found that it was more computationally costly and not more effective at cluster detection than the MF method. Throughout this work, our MCMC is run over a relatively small area of sky (512 pixels × 512 pixels, or $\sim 2^\circ \times 2^\circ$) centered on a cluster that has already been identified.

Cluster parameter recovery is tested in single- and multi-frequency simulations below (Section 5), but we use only 150 GHz when investigating scaling relations (for observed and simulated clusters) to match the SPT cluster analysis in B13, from which our sample is derived. We use the β-model source template given in Equation (2). T. E. Montroy et al. (2015, in preparation) demonstrate, using simulations and methods similar to those described in Section 5, that $Y_{\rm SZ}$ is recovered accurately with a β-model for either β-model or Arnaud profile (Arnaud et al. 2010) input clusters.

Clusters, as described by the β-model, are characterized by four parameters: their location on the sky in R.A. and decl., the magnitude of the SZ temperature decrement ΔT_0, and the core radius $\theta_{\rm c}$. We apply priors in the form of uniform probability distributions in each parameter. Given that we are characterizing clusters that have already been detected by the MF, our position priors can be quite tight. We impose a simple square-box prior on R.A. and decl., centered at the MF cluster location and extending $\pm 1\farcm25$. Our ΔT_0 and $\theta_{\rm c}$ priors restrict these parameters to broadly reasonable values given the expected mass and redshift range of our cluster sample. Our SZ temperature decrement prior is $-2.5\,{\rm mK} \leqslant \Delta T_0 \leqslant 0.0\,{\rm mK}$, and our radius prior is $0\farcm025 \leqslant \theta_{\rm c} \leqslant 2\farcm5$. $\theta_{\rm c}$ is not allowed to fall to zero for numerical reasons.

For a detailed examination of the SPT beam functions and noise properties, see Schaffer et al. (2011). Figure 2 of that work shows how the SPT beams scale with physical radius and ℓ. Figure 7 shows the signal+noise and noise PSDs for an SPT map, both from the raw map, and corrected for the beam and transfer functions.

Burn-in, as evaluated by stability of the likelihood values, is typically complete within several hundred steps. For the 12,000 simulated cluster realizations in Section 5, we cut the first 10^3 steps, using the rest of the 10^4 steps to characterize the probability surface. In the scaling relation analysis discussed in Section 6 many fewer clusters were analyzed, allowing the chain length to be extended to 10^5 steps, from which we exclude the first 10^4 steps in order to ensure convergence. We define recovered parameter values to be the median of the MCMC equilibrium distribution for each parameter, marginalizing over the other parameters. Uncertainties are given by the 68% confidence interval of the marginalized distribution for each parameter, centered on the median value. Figure 1 shows the parameter distributions for a typical cluster detected with the SPT.

4. SIMULATIONS

4.1. Simulated Thermal SZ Cluster Maps

We used two sets of simulations: one uses β-model clusters (defined by ΔT_0 and $\theta_{\rm c}$) to investigate cluster parameter recovery (Section 5), while the second uses cluster gas profiles inferred from dark matter light cone simulations to calibrate $Y_{\rm SZ}$–M scaling relations (Section 6). The second set of simulations is described in detail in Shaw et al. (2010) and will be referred to as the S10 simulations for convenience. The thermal SZ (tSZ) cluster profiles used in each set are discussed in more detail in the relevant sections below.

4.2. Astrophysical Backgrounds

We use simulated maps of astrophysical backgrounds that include contributions from the CMB and extragalactic point sources. Simulated CMB anisotropies were generated based on realizations of the gravitationally lensed *WMAP* 5 yr ΛCDM CMB power spectrum.

The extragalactic point source population at 150 GHz consists of two classes of objects: "dusty" sources dominated by thermal dust emission from star formation bursts, and "radio" sources dominated by synchrotron emission. We use the source count model of Negrello et al. (2007) at 350 GHz, which is based on physical modeling by Granato et al. (2004) for dusty sources. Source counts at 150 GHz are estimated by assuming the flux densities scale as $S_\nu \propto \nu^\alpha$, where $\alpha = 3$ for high-redshift protospheroidal galaxies, and $\alpha = 2$ for late-type galaxies. For radio sources we use the De Zotti et al. (2005) model at 150 GHz, which is in agreement with observed radio source populations at $S < 100$ mJy (Vieira et al. 2010; Marriage et al. 2011; Planck Collaboration et al. 2011a; Marsden et al. 2013; Mocanu et al. 2013).

Point source population realizations were generated by sampling from Poisson distributions for each population in bins with fluxes from 0.01 mJy to 1000 mJy. Sources were randomly distributed across the map. Correlations between sources or with galaxy clusters were not modeled, following V10. These 150 GHz simulated point source populations were used for the scaling relation simulations of Section 6, but not for the multi-band pipeline checks of Section 5.

4.3. Simulated Observations

Ideally, we could emulate the SPT transfer function for the 95 GHz and 150 GHz frequency bands by producing

[38] Mathworks Inc., Natick, MA 01760, USA.

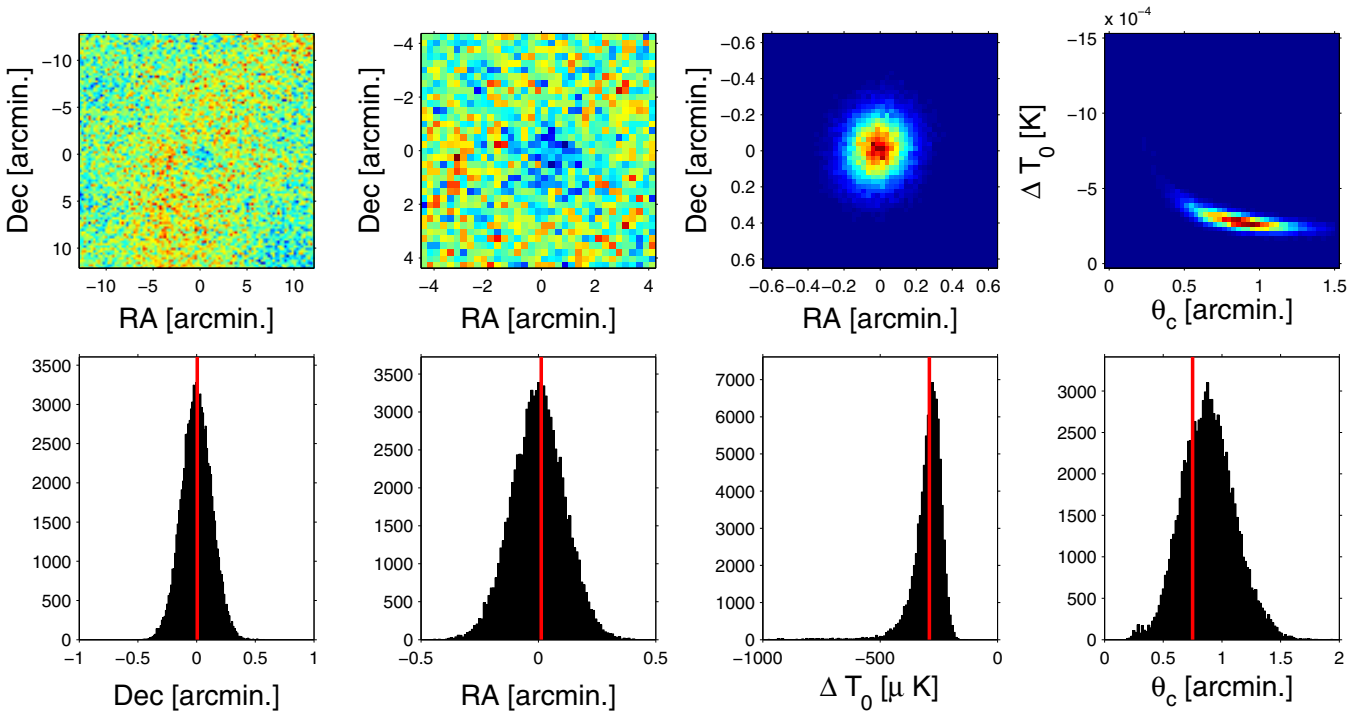

Figure 1. From left to right; the top row shows (1) a $25' \times 25'$ section of an SPT sky map centered on cluster SPT-CL J2341-5119 ($\xi = 9.65$, $z = 0.9983$); (2) a close up of $7.'5 \times 7.'5$ centered on the cluster location, (3) the estimated posterior distribution of the cluster position, marginalizing over ΔT_0; and θ_c, and (4) the estimated posterior distribution of ΔT_0 and θ_c, marginalizing over position. Likewise, the bottom row shows one-dimensional marginalized distributions of the parameters. (5) Declination, (6) right ascension, (7) ΔT_0, and (8) θ_c. Vertical red lines in the bottom row indicate the matched filter parameter values for this cluster.

synthetic timestreams from simulated maps convolved with the SPT beam, observing them using the SPT scan strategy, and convolving the resulting timestreams with detector time constants. We would then produce maps by processing the simulated timestreams as in Section 2.1. However, this full emulation of the SPT transfer function is computationally intensive. To simplify this process and produce a large number of sky maps, we model the transfer function as a two-dimensional Fourier filter. V10 show that this approximation introduces systematic errors in the recovered cluster ξ values of less than 1%.

The instrumental and atmospheric noise in the SPT maps were estimated by creating difference maps, which were constructed to have no astrophysical signal. Each field consists of several hundred individual observations. We randomly multiply half of the observations by -1, and then coadd the full set of observations. We repeat this several hundred times, each time calculating the two-dimensional spatial power spectrum, which we average to estimate the instrumental and atmospheric noise in the coadded SPT map. This averaged noise spectrum is used to generate random map realizations of the SPT noise, which are added to the simulated maps.

5. PIPELINE CHECKS

5.1. Cluster Model

We use mock observations of clusters in simulated sky maps to evaluate the accuracy and bias of the recovered cluster parameters. We begin with simulated maps that contain the astrophysical signals described in Section 4.2. To this we add mock clusters with an assumed β-model profile, with known SZ decrements and radii, at specified locations. Simulated SPT observations are then performed on these maps. Three different cluster core radii ($0.'25$, $0.'5$, and $1.'0$) are used, combined with eight values for peak Comptonization between 175 μK and 2 mK, spanning the range of values typically found for SPT-detected clusters with $\xi > 5$. These cluster profiles are convolved with the SPT transfer function, and then placed in the simulated maps. For each combination of β-model cluster parameters, we create five pairs of simulated maps (150 GHz and 95 GHz) by placing 100 copies of the cluster at random locations in five unique noise maps. This results in 500 noise realizations for each combination of cluster parameters, or 12,000 clusters total. As usual, $\sim 2^\circ \times 2^\circ$ cutouts are made around each cluster, and the MCMC is run on each patch.

In Sections 5.2 and 5.3, we test parameter recovery in the single-band (150 GHz) and multiband (95 GHz and 150 GHz) cases. The 220 GHz data contain no SZ information, but could in principle be used to remove primordial CMB anisotropy. However, the noise level of the 220 GHz maps, dominated by residual atmospheric emission, is larger than the intrinsic astrophysical confusion caused by CMB anisotropy. Therefore, we do not use the 220 GHz SPT measurements to fit the cluster model.

5.2. Position, Radius, and Amplitude

We first examine the recovered values of the four baseline cluster parameters: the R.A. and decl. position, ΔT_0, and θ_c. The cluster positions are measured accurately, and we find no bias in either position parameter, for both the single-band and multiband cases. For clusters near the SPT beam size ($\sim 1'$ FWHM at 150 GHz) and selection threshold, the amplitude and shape of the cluster will not be well constrained, however the integrated signal within the SPT beam will be. A similar degeneracy has previously been noted in other cluster analyses (e.g., Benson et al. 2004; Planck Collaboration et al. 2011a, 2013a). In Figure 2, we show the recovered ΔT_0 and θ_c

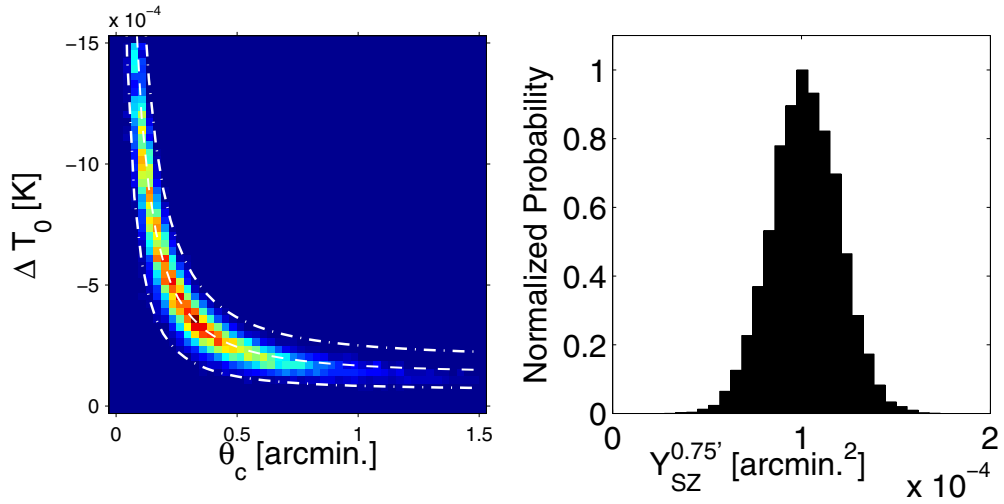

Figure 2. SPT-CL J0533-5005 ($\xi = 5.59$, $z = 0.8810$), an SPT observed cluster with core radius $\theta_c < 1'$. The left figure shows the estimated posterior distribution of ΔT_0 and θ_c, and the right figure shows the posterior distribution of Y_{SZ} calculated from the $\Delta T_0 + \theta_c$ distribution. For clusters near the SPT beam size ($\sim 1'$ FWHM at 150 GHz) and selection threshold, the position is well constrained; however, the radius and amplitude are degenerate. Despite this, the integrated Comptonization, Y_{SZ}, is well constrained. The overplotted curves in the left figure are Y_{SZ} iso-curves. The dashed line is the recovered Y_{SZ} for this cluster, while the dot-dashed lines are $\pm 50\%$ Y_{SZ}.

distributions for a typical cluster in the SPT catalog (SPT-CL J0533-5005, $\xi = 5.59$, $z = 0.8810$, $\theta_c < 1'.0$). While the position is well-constrained, there is a significant degeneracy between the constraints on θ_c and ΔT_0.

5.3. Integrated Comptonization

In general, the cylindrically projected integrated Comptonization of a cluster is calculated by integrating the source function, $S(\theta)$, out to a given angular aperture θ_{int}:

$$Y_{SZ} = 2\pi \int_0^{\theta_{int}} S(\theta)\theta \, d\theta. \quad (7)$$

For much of this work, θ_{int} will be a constant angular aperture. We distinguish this estimator of Y_{SZ} from others by referring to it as Y^{θ}_{SZ} hereafter.

In the case of a two-dimensional projection of a spherical β-model with $\beta = 1$ (Equation (2)), this integral can be solved analytically:

$$Y^{\theta}_{SZ} = \frac{\pi \Delta T_0 \theta_c^2}{f_x T_{CMB}} \log\left[1 + \left(\frac{\theta_{int}}{\theta_c}\right)^2\right], \quad (8)$$

where θ_c is the core radius in arcminutes, ΔT_0 is the central temperature decrement in units of K_{CMB}, the equivalent CMB temperature fluctuation required to produce the observed power fluctuation, T_{CMB} is the CMB blackbody temperature of 2.725 K, and f_x is given by

$$f_x = \left(x \frac{e^x + 1}{e^x - 1} - 4\right)[1 + \delta(x, T_e)], \quad (9)$$

where $x = h\nu / kT_{CMB}$, and $\delta(x, T_e)$ accounts for relativistic corrections to the SZ spectrum (Itoh et al. 1998; Nozawa et al. 2000). For the details of the calculation of f_x for the SPT, see A11.

We use this equation to calculate Y^{θ}_{SZ} for every step in the MCMC chain, and thus to produce a marginalized distribution of Y^{θ}_{SZ} values. In these simulations, integration to a radius approximately corresponding to the 150 GHz SPT beam diameter (roughly the range $0'.75 < \theta_{int} < 1'.25$) produces Y^{θ}_{SZ} distributions that are well constrained despite the degeneracy of θ_c and ΔT_0, with minimal error in recovered cluster Y^{θ}_{SZ} values. Integration in this section is performed to $\theta_{int} = 0'.75$, though other values are explored for scaling relations in Section 6 below. Note that we calculate Y^{θ}_{SZ} from the marginalized distribution of the source model parameters, not by integrating the flux on the sky. It is also important to note that the likelihood is calculated (in frequency space) over the full $2^\circ \times 2^\circ$ patch of sky, θ_{int} is simply the radius out to which the best fit β-model is integrated.

If the redshift of a cluster is known, it is also possible to integrate Y_{SZ} within an angular aperture corresponding to a specific physical radius, ρ:

$$\theta_{int} = \rho \, D_A^{-1}(z),$$

where $D_A(z)$ is the angular diameter distance to the redshift z. In Sections 6 and 7, we examine Y_{SZ} integrated within a constant physical radius, ρ, for all clusters in a sample. We will refer to this quantity as Y^{ρ}_{SZ}.

In Figure 2, we show a typical SPT cluster in which Y^{θ}_{SZ} is well constrained despite the degeneracy between ΔT_0 and θ_c. Figure 3 shows Y_{SZ} and θ_c parameter distributions for 500 runs of a typical simulated cluster with a radius smaller than the SPT 150 GHz beam size ($\theta_c = 0'.5$, $\Delta T_0 = 300\,\mu$K, $\xi = 6.2$). The 68% confidence interval for Y_{SZ} in these simulations is typically $\sim$14% of the central value. The cutoff at low θ_c is due to the small, but non-zero, minimum priors on θ_c and ΔT_0, this is not a feature of the data likelihood. Despite only having an upper bound on θ_c, Y_{SZ} is still well constrained. We find that Y_{SZ} is well constrained and consistent regardless of whether the analysis is single-band (150 GHz) or multiband (95 GHz and 150 GHz).

In Figure 4, we show the ratio of the recovered to input Y_{SZ} as a function of core radius and cluster detection significance, ξ, for 24 different combinations of θ_c and ΔT_0, each with 500 independent noise realizations. Despite a slight apparent bias for some θ_c values, we find no significant bias as a function of the detection significance, and recover Y_{SZ} accurately to <2% in all cases. On average recovered Y^{θ}_{SZ} values are 0.27% lower than input values, which is below the 0.49% error in the mean.

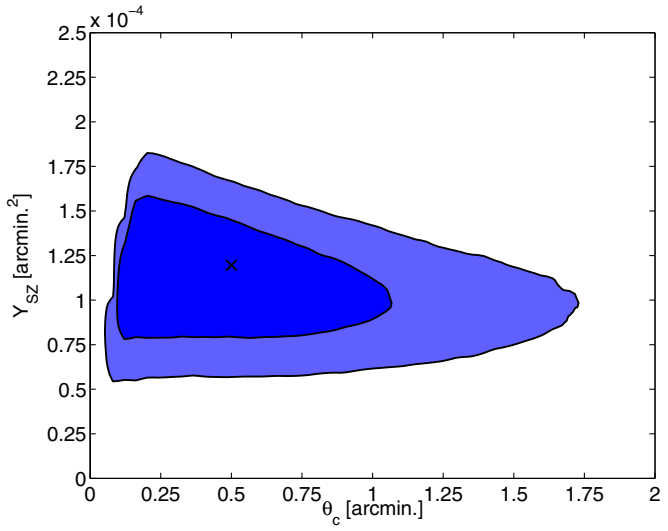

Figure 3. The marginalized constraints on Y_{SZ} and θ_c from 500 noise realizations of a typical simulated cluster with radius smaller than the SPT 150 GHz beam ($\theta_c = 0.'5$, $\Delta T_0 = 300\,\mu$K, $\xi = 6.2$). The contours show the 68% and 95% confidence regions. The cross marks the input θ_c and Y_{SZ} values ($Y_{SZ}^{0.'75} = 1.20 \times 10^{-4}$ arcmin^2). Despite only having an upper bound on θ_c, Y_{SZ} is well constrained.

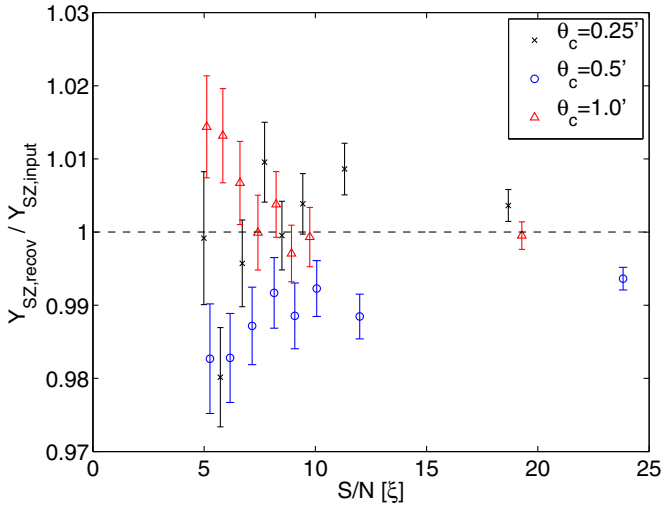

Figure 4. Average ratios of recovered to input Y_{SZ} for 24 β-model source profiles, generated from different combinations of θ_c and ΔT_0. Each point is the mean recovered Y_{SZ} for a simulated cluster with 500 independent noise realizations. The errorbars represent the error on the mean of these recovered Y_{SZ} values.

6. SCALING RELATIONS FROM SIMULATED CLUSTERS

In this section, we compare Y_{SZ} and ζ as SZ observables for the SPT-SZ survey, focusing on their scatter with cluster mass. To do this, we use maps derived from the S10 simulations, which are intended to provide more realistic cluster profiles than the β-model clusters used in Section 5.

The steepness of the galaxy cluster mass function will introduce bias in a scaling relation fitted in the presence of noise or intrinsic scatter in the population. Therefore, in Section 6.3 we fit Y_{SZ}^{θ}–M scaling relations for clusters in simulated tSZ-only maps, to minimize the selection bias. These maps contain none of the celestial or instrumental noise spectra described in Section 4 (CMB, point sources, atmospheric noise, and instrumental noise), only tSZ signal.

In Section 6.4, we fit for a Y_{SZ}^{θ}–M scaling relation using clusters in S10 simulation maps containing the full astrophysical and instrumental noise terms to evaluate the performance of the MCMC in the presence of noise. The main reason to consider intrinsic and measurement error is that both are important in terms of the cosmological analysis. For example, both intrinsic and measurement uncertainty affect the selection of the cluster sample: a larger measurement uncertainty would cause lower mass clusters to scatter into the cluster sample, decreasing the purity. Therefore we consider the total scatter, which includes both sources, to evaluate the performance of our method.

6.1. Simulated Clusters

The S10 simulations are based on a dark matter lightcone simulation, with cosmological parameters consistent with the *WMAP* 5 yr data and large-scale structure measurements (Dunkley et al. 2009). To include baryons in the simulations, Shaw et al. (2010) apply the semi-analytic gas model of Bode et al. (2007), specifically their fiducial model, to the dark matter halos identified in the output of the lightcone simulation. From the simulations, we construct two-dimensional SZ intensity maps at 150 GHz of clusters with virial mass (M_{vir}) greater than $5 \times 10^{13} M_{\odot}\, h^{-1}$ by summing the electron pressure density along the line of sight. The resulting maps are projections of all the clusters in the lightcone simulation onto a simulated sky. Forty $10^{\circ} \times 10^{\circ}$ maps were produced by this procedure, together with catalogs of cluster masses, redshifts, and positions.

6.2. Y_{SZ}–M Scaling Relation Fitting Methods

We assume a scaling between Y_{SZ} and M of the form

$$Y_{SZ} = A_{SZ} \left(\frac{M_{vir}}{3 \times 10^{14}\, M_{\odot}\, h^{-1}} \right)^{B_{SZ}} \left(\frac{E(z)}{E(0.6)} \right)^{C_{SZ}}, \quad (10)$$

parameterized by the normalization A_{SZ}, the mass scaling B_{SZ}, and the redshift evolution C_{SZ}, and where $E(z) \equiv H(z)/H_0$. For self-similar evolution, $B_{SZ} = 5/3$ and $C_{SZ} = 2/3$ (e.g., Kravtsov et al. 2006). The pivot points of the scaling relation were defined to match the approximate mean mass and redshift for the SPT cluster sample.

We fit the Y_{SZ}^{θ}–M_{vir} scaling relation by minimizing the fractional scatter, $\mathcal{S}$, in Y_{SZ}^{θ}, defined as

$$\mathcal{S} = \sqrt{\frac{1}{N} \sum_{n=1}^{N} \left(\frac{Y_n^{recov} - Y_n^{input}}{Y_n^{input}} \right)^2}, \quad (11)$$

where Y_n^{recov} is the integrated Comptonization recovered by the MCMC for the nth cluster, Y_n^{input} is the corresponding Comptonization calculated from the input catalog mass and the assumed scaling relation (Equation (10)), and we sum over N simulated clusters. The scaling relation parameters A_{SZ}, B_{SZ}, and C_{SZ} are varied using a grid search method, and the scatter $\mathcal{S}$ is calculated at each point in the parameter space. The combination of parameters that minimizes $\mathcal{S}$ is taken to be the best-fit set of parameters. This definition of fractional scatter is used to fit Y_{SZ}^{θ}–M_{vir} scaling relations in Section 6.3 and in Section 6.4.

6.3. Results for Simulated Thermal-SZ-only Maps

We run both the MCMC and MF methods on tSZ-only maps from the S10 dark matter lightcone simulations described in

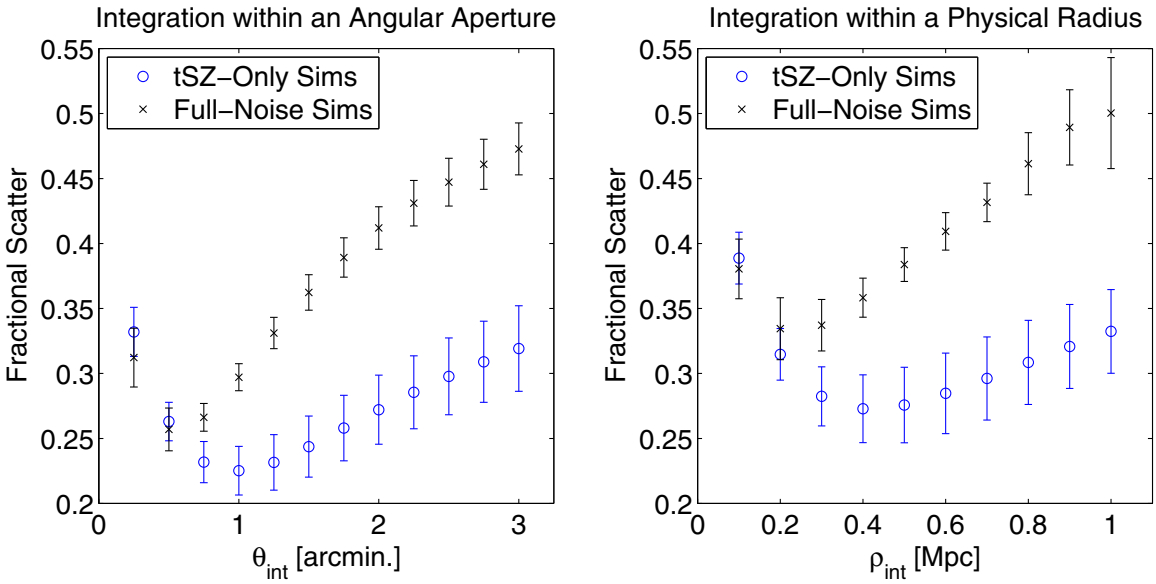

Figure 5. Fractional scatter vs. integration radius for tSZ-only and full noise simulations. Left panel: fractional scatter vs. integration angle in arcminutes. Right panel: fractional scatter vs. integration radius in megaparsecs. The scatter in the tSZ-only simulations is essentially the intrinsic scatter in the population since only tSZ fluctuations are present. Adding the other noise terms shifts the scatter up, and the minimum down in angular or physical scale because those noise terms dominate at large angles. The optimal angular apertures correspond roughly to the optimal physical radii at the median redshift of the cluster sample, $z = 0.6$.

Section 6.1. These simulated tSZ maps contain only tSZ signal, and no CMB, point sources, atmospheric noise, or instrumental noise.

We measure the SZ signal in these maps using the methods described in Sections 5.1 and 5.3 for clusters with $M_{\rm vir} > 4 \times 10^{14} M_{\odot}\, h^{-1}$, and redshift $0.3 < z < 1.2$. We then use the cluster virial masses and Equation (10) to find the best-fit scaling relation parameters by minimizing the fractional scatter in Equation (11). We do this for both the $Y_{\rm SZ}$–$M_{\rm vir}$ and ζ–$M_{\rm vir}$ scaling relations, which allows for direct comparison of these analysis methods. The redshift range corresponds to the redshift range of observed SPT clusters, and the mass criteria correspond to the mass of clusters at the lower SPT significance limit of the Reichardt et al. (2013) cluster catalog ($\xi = 4.5$), at the survey median redshift of $z = 0.6$.

As a baseline for the scatter in the measured $Y_{\rm SZ}$–$M_{\rm vir}$ scaling relations for these simulations, we examine the intrinsic scatter between $M_{\rm vir}$ and $Y_{\rm vir}$, the contribution to the SZ flux from within the spherical virial radius for each cluster. We fit the $Y_{\rm vir}$–$M_{\rm vir}$ scaling relation parameters using the same method as for measured $Y_{\rm SZ}$ values, and find the fractional scatter in the best-fit scaling relation to be 16%.

We fit $Y^{\theta}_{\rm SZ}$–$M_{\rm vir}$ relations for a range of angular apertures, θ, with $Y^{\theta}_{\rm SZ}$ defined in Equation (8). Figure 5 shows the fractional scatter as a function of the integration angle for angles ranging from 0.′25 to 3.′0. We find that the fractional scatter in $Y^{\theta}_{\rm SZ}$ does not vary significantly with angular aperture, with a broad minimum in the scatter at ∼0.′75–1.′0 ($Y^{0.'75}_{\rm SZ}$). The exact location of the minimum scatter shifts between the tSZ-only maps and the full-noise S10 maps, but is near 0.′75 in both cases (see Figure 5). For simplicity, and for comparison between the different simulated maps and observed clusters, we use the $Y^{0.'75}_{\rm SZ}$–$M_{\rm vir}$ scaling relation as our nominal scaling relation. The $Y^{0.'75}_{\rm SZ}$–$M_{\rm vir}$ scaling relation has 23% ± 2% fractional scatter in $Y_{\rm SZ}$, which is slightly less than the 27% ± 2% scatter in the ζ–$M_{\rm vir}$ scaling relation for these clusters. The scatter in the tSZ-only simulations is primarily due to the intrinsic scatter in the mass to SZ observable scaling, scatter from the tSZ background is sub-dominant. (Note that the scatter here is fractional scatter, whereas previous SPT analyses in V10 and B13 quoted a log-normal scatter, at a level consistent with the values found in this work.)

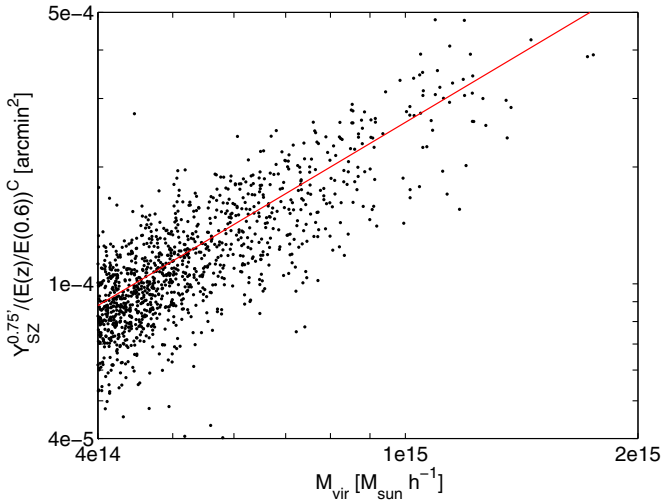

Figure 6. $Y^{0.'75}_{\rm SZ}$ vs. $M_{\rm vir}$ for 1187 mass-selected clusters in the S10 simulated tSZ-only maps, where we only include clusters with $M_{\rm vir} > 4 \times 10^{14} M_{\odot}\, h^{-1}$ in the redshift range $0.3 < z < 1.2$. Fractional scatter in $Y_{\rm SZ}$ is 23% ± 2%. The solid line is the best-fit $Y^{0.'75}_{\rm SZ}$–$M_{\rm vir}$ scaling relation found for this cluster sample.

Figure 6 shows $Y^{0.'75}_{\rm SZ}$ versus $M_{\rm vir}$ for the 1187 clusters examined from this simulation. The solid line is the best-fit $Y^{0.'75}_{\rm SZ}$–$M_{\rm vir}$ scaling relation found for these clusters. The scaling relation parameters ($A_{\rm SZ}$, $B_{\rm SZ}$, $C_{\rm SZ}$, and $\mathcal{S}$) for the $Y^{0.'75}_{\rm SZ}$ scaling relation are given in Table 1.

We also calculate $Y_{\rm SZ}$ within a constant physical radius, ρ, ($Y^{\rho}_{\rm SZ}$) for all the clusters in the catalog. The angular size of a cluster is a function of its redshift; therefore, it is interesting

Table 1
Y_{SZ}–M Scaling Relation Parameters

Data Set	MCMC					MF
	Integration Radius	A_{SZ} ($\times 10^{-4}$)	B_{SZ}	C_{SZ}	Scatter	Scatter
tSZ-only S10 sims	0.′75	1.44 ± 0.11	1.20 ± 0.11	1.63 ± 0.24	$23\% \pm 2\%$	$27\% \pm 2\%$
	0.3 Mpc	1.53 ± 0.16	1.26 ± 0.17	1.13 ± 0.13	$28\% \pm 2\%$	
Full-noise S10 sims	0.′75	1.37 ± 0.10	1.04 ± 0.11	1.02 ± 0.20	$27\% \pm 1\%$	$27\% \pm 2\%$
	0.3 Mpc	1.49 ± 0.18	1.12 ± 0.22	0.53 ± 0.25	$34\% \pm 2\%$	
B13 SPT observed clusters	0.′75	1.85 ± 0.36	1.77 ± 0.35	0.96 ± 0.50	$21\% \pm 11\%$[a]	$21\% \pm 9\%$[a]
	0.3 Mpc	2.09 ± 0.35	1.43 ± 0.20	0.35 ± 0.28	$26\% \pm 9\%$[a]	

Notes. The tSZ-only maps contain only thermal SZ signal, while the full-noise S10 maps include tSZ, CMB, point sources, atmospheric noise, and realistic SPT instrumental noise. The values of scatter reported for the simulations are fractional scatter, while the values reported for the B13 clusters are intrinsic log-normal scatter. In the S10 simulations virial masses are used to fit the scaling relations, while for the B13 cluster sample the masses are M_{500}. For comparison with the scatter in each Y_{SZ}–M scaling relation we list the scatter in the corresponding MF derived ζ–M scaling relation for the same data set.
[a] These values are intrinsic log-normal scatter.

to measure Y_{SZ} within a fixed physical radius. In Figure 5, we plot the best-fit scatter for a range of integration radii between 0.1 and 1.0 Mpc. We find that the minimum fractional scatter in Y_{SZ} within a fixed physical radius is higher than the minimum fractional scatter within a fixed angular aperture. For Y^{ρ}_{SZ}, the scatter is increased by the varying angular size of the chosen physical radius at different redshifts. The optimal physical radius corresponds roughly to the optimal angular aperture, at the median redshift of the cluster sample, $z = 0.6$. Clusters farther from the median redshift will have integration angles farther from the optimal angle, resulting in relatively higher scatter in Y^{ρ}_{SZ} than in Y^{θ}_{SZ}.

As can be seen in Figure 5, we find a broad minimum in scatter at ∼0.3–0.4 Mpc, with a minimum scatter of $27\% \pm 3\%$. This is comparable to the ζ–M_{vir} relation for these clusters, and slightly higher than the scatter in the $Y^{0.'75}_{SZ}$–M_{vir} scaling relation. The scaling relation parameters for Y_{SZ} within 0.3 Mpc ($Y^{0.3\,Mpc}_{SZ}$; 0.3 Mpc being equivalent to 0.′75 at $z = 0.6$) are given in Table 1.

6.4. Results for Full-noise Simulated Maps

We also fit Y^{θ}_{SZ}–M_{vir} scaling relations for the simulated clusters in the presence of other astrophysical and instrumental noise components (see Sections 4.2 and 4.3). The same cluster sample ($M_{vir} > 4 \times 10^{14} M_{\odot}\, h^{-1}$, and $0.3 < z < 1.2$) was analyzed in this set of simulations as in the simulated tSZ-only maps. We will refer to this set of simulations as the full-noise S10 simulated maps. These simulations are important for understanding the cluster sample selection, which will be affected by the total noise.

The scaling relation fitting for the clusters from this set of simulations was performed as in Section 6.3. As in Section 6.3, the scatter is a weak function of angular aperture, with the minimum shifted to ∼0.′5–0.′75. Figure 5 shows the fractional scatter as a function of angular aperture of integration.

For the $Y^{0.'75}_{SZ}$–M_{vir} scaling relation we find a fractional scatter in Y_{SZ} of $27\% \pm 1\%$. Since the scatter here includes both intrinsic scatter and the measurement uncertainty, we expect it to be larger than the scatter in $Y^{0.'75}_{SZ}$ in Section 6.3. This level of scatter is comparable to the $27\% \pm 2\%$ scatter in ζ found in the ζ–M_{vir} scaling relation for these simulations.

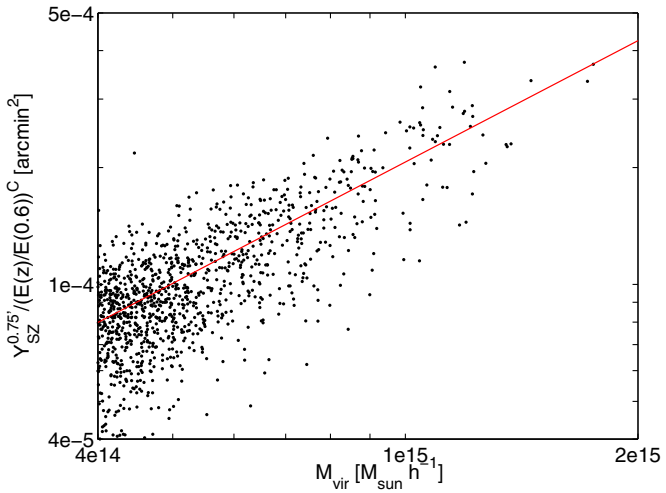

Figure 7. $Y^{0.'75}_{SZ}$ vs. M_{vir} for 1187 mass-selected clusters in the full-noise S10 simulations, which include CMB, point sources, astrophysical noise, and realistic SPT instrument noise. We include only clusters with $M_{vir} > 4 \times 10^{14} M_{\odot}\, h^{-1}$ in the redshift range $0.3 < z < 1.2$. Fractional scatter in Y_{SZ} is $27\% \pm 1\%$. The solid line is the best-fit $Y^{0.'75}_{SZ}$–M_{vir} scaling relation found for this cluster sample.

Figure 7 shows $Y^{0.'75}_{SZ}$ versus M_{vir} for the 1187 clusters analyzed from the full-noise S10 simulated maps. The solid line is the best-fit $Y^{0.'75}_{SZ}$–M_{vir} scaling relation found for this cluster sample. The mass scaling relation parameters for $Y^{0.'75}_{SZ}$ in this set of simulations are given in Table 1. It will be noted that some of the scaling relation parameters here differ significantly from those in the tSZ-only simulations in Section 6.3. This is expected because intrinsic and measurement scatter are not distinguished here. The full cosmoMC treatment of the data in Section 7 deals with these issues. The scaling relation values from that section are the most accurate. The results in this section are meant to be illustrative only.

Using these simulations we also calculate Y^{ρ}_{SZ} for a range of ρ values, as in Section 6.3, and fit Y^{ρ}_{SZ}–M_{vir} scaling relations for each ρ. Figure 5 shows the fractional scatter as a function of the integration radius for a range of physical radii. We find a broad minimum in scatter at ∼0.2–0.3 Mpc, with a minimum scatter of $33\% \pm 2\%$. The optimal integration radius shifts down

Table 2
SPT Cluster Fluxes and Masses

Object Name	z	$Y_{SZ}^{0'.75}$ ($10^{14} M_\odot$ keV)	Y_{SZ}^{500} ($10^{14} M_\odot$ keV)	Y_X ($10^{14} M_\odot$ keV)	M_{SZ}^{500} ($10^{14} M_\odot\, h_{70}^{-1}$)	M_X^{500} ($10^{14} M_\odot\, h_{70}^{-1}$)
SPT-CL J0509-5342	0.463	0.9 ± 0.1	$3.6^{+1.4}_{-1.1}$	4.3 ± 0.8	4.32 ± 1.11	5.11 ± 0.75
SPT-CL J0511-5154[a]	0.74	1.2 ± 0.2	...	...	2.79 ± 1.43	...
SPT-CL J0521-5104[a]	0.72	1.1 ± 0.2	...	...	2.46 ± 1.32	...
SPT-CL J0528-5259	0.765	1.1 ± 0.2	$1.8^{+0.8}_{-0.5}$	1.6 ± 0.5	2.21 ± 1.14	2.54 ± 0.54
SPT-CL J0533-5005	0.881	1.4 ± 0.2	$2.1^{+0.6}_{-0.4}$	1.0 ± 0.4	2.75 ± 1.39	1.86 ± 0.43
SPT-CL J0539-5744[a]	0.77	1.0 ± 0.2	...	...	1.93 ± 0.93	...
SPT-CL J0546-5345	1.067	2.0 ± 0.3	$5.0^{+1.1}_{-1.0}$	4.8 ± 0.8	4.18 ± 0.89	4.79 ± 0.86
SPT-CL J0551-5709	0.423	0.7 ± 0.1	$3.4^{+1.7}_{-1.2}$	1.9 ± 0.4	3.57 ± 1.43	3.32 ± 0.46
SPT-CL J0559-5249	0.611	1.6 ± 0.2	$9.0^{+2.1}_{-1.8}$	6.4 ± 0.8	5.46 ± 1.04	6.29 ± 0.86
SPT-CL J2301-5546[a]	0.748	1.0 ± 0.2	...	...	1.89 ± 0.89	...
SPT-CL J2331-5051	0.571	1.4 ± 0.2	$2.3^{+0.4}_{-0.3}$	3.5 ± 0.6	5.29 ± 1.00	4.50 ± 0.64
SPT-CL J2332-5358	0.403	$0.9^{+0.2}_{-0.1}$	$8.7^{+3.7}_{-3.1}$	6.1 ± 0.8	5.25 ± 1.04	6.39 ± 0.75
SPT-CL J2337-5942	0.781	3.1 ± 0.2	$7.8^{+1.3}_{-1.4}$	8.5 ± 1.7	6.67 ± 1.29	6.82 ± 1.11
SPT-CL J2341-5119	0.998	2.3 ± 0.2	6.8 ± 1.1	4.7 ± 1.0	4.86 ± 0.93	4.64 ± 0.86
SPT-CL J2342-5411	0.074	1.5 ± 0.3	2.6 ± 0.6	1.4 ± 0.3	2.46 ± 1.32	2.36 ± 0.43
SPT-CL J2355-5056	0.320	0.4 ± 0.1	$2.1^{+0.9}_{-0.7}$	2.2 ± 0.4	3.11 ± 1.61	3.75 ± 0.46
SPT-CL J2359-5009	0.774	1.4 ± 0.2	$4.5^{+1.3}_{-1.1}$	1.8 ± 0.4	3.61 ± 1.11	2.86 ± 0.50
SPT-CL J0000-5748	0.701	1.1 ± 0.2	$2.1^{+1.1}_{-0.6}$	4.2 ± 1.6	2.57 ± 1.36	4.14 ± 0.93

Notes. Cluster redshifts and X-ray fluxes are quoted from Benson et al. (2013). $Y_{SZ}^{0'.75}$ is the integrated Comptonization within 0'.75, calculated with our Y_{SZ} MCMC method. Y_{SZ}^{500} is the integrated Comptonization within r_{500}. $Y_{SZ}^{0'.75}$ and Y_{SZ}^{500} values are given in $M_\odot$ keV for comparison to Y_X and the Y_{SZ} values from A11. $Y_{SZ}^{0'.75}$ and Y_{SZ}^{500} are cylindrically projected. M_{SZ}^{500} and M_X^{500} are estimates of M_{500} calculated from the same CosmoMC chains, using only the $Y_{SZ}^{0'.75}$ and Y_X data, respectively.
[a] These clusters have only SZ data, and no X-ray observations.

here relative to the simulated tSZ-only maps because of the scale dependence of the noise sources added in the full-noise S10 maps, which dominate the scatter in these simulations. In particular, the noise induced by the simulated CMB increases with angular scale, leading to a preference for smaller integration radii. The scatter in Y_{SZ}^{ρ} for these simulations is slightly higher than the scatter in both the ζ and the $Y_{SZ}^{0'.75}$ mass scaling relations. The scaling relation parameters for the nominal $Y_{SZ}^{0.3\,\mathrm{Mpc}}$ mass scaling relation are given in Table 1. The optimal physical radius again corresponds roughly to the optimal angular aperture, at the median redshift of the cluster sample.

7. Y_{SZ} FOR SPT OBSERVED CLUSTERS

7.1. Y_{SZ}–M_{500} Scaling Relation Fitting Methods

In this section, we perform Y_{SZ}^{θ}–M scaling relation fitting for a sample of SPT observed clusters, using the same scaling relation as in the simulations (Equation (10)) and the X-ray determined cluster masses. We use only 150 GHz data in this section to be directly comparable to the results in Benson et al. (2013), which does not include 95 GHz data. In this section, we define cluster mass as M_{500}, the mass inside a spherical radius r_{500}, within which the average density is 500 times the critical density of the universe at the cluster's redshift. To fit this scaling relation with clusters selected in the SPT-SZ survey, we have to account for the shape of the cluster mass function and the SPT survey selection, which was based on the SPT significance, ξ. This is similar to the procedure followed in previous SPT analyses (Reichardt et al. 2013; B13; V10), with the added complication that in this work we must express the SPT selection function in Y_{SZ} instead of ξ.

The (unnormalized) probability of a mass M given an integrated Comptonization Y_{SZ} is given by

$$\overline{\mathrm{P}}(M|Y_{SZ}) = P(Y_{SZ}|M)P(M),$$

where $P(Y_{SZ}|M)$ is the Gaussian probability distribution with which we have been working previously, and $P(M)$ is the mass function. The number of clusters is a steep function of cluster mass, which (combined with the measurement uncertainty in Y_{SZ}) results in relatively more low-mass than high-mass clusters at a given Y_{SZ}, an effect commonly referred to as Eddington bias.

For our cluster sample we use the 18 clusters from B13, 14 of which have X-ray derived masses (see Section 2.3), and all of which have $\xi > 5$. For this analysis we use only the 150 GHz data, the SPT band with the highest SZ sensitivity. For a list of cluster names, ξ values, and redshifts for this sample, see Table 2.

To fit for scaling relations, we use a method similar to the one described in B13, which we modify to account for the cluster selection based on Y_{SZ} instead of ζ. In B13, we used a version of the CosmoMC (Lewis & Bridle 2002) analysis package, modified to include the cluster abundance likelihood in the CosmoMC likelihood calculation. All fitting is performed assuming a standard flat ΛCDM cosmology, parameterized with the standard six-parameters ($\Omega_c h^2$, $\Omega_b h^2$, Θ_s, n_s, Δ_R^2, and τ), and using the *WMAP* 7 yr data set. The cosmological parameters are held constant throughout, we marginalize over only the cluster scaling relation parameters. At each step in the chain, a point in the joint cosmological and scaling relation parameter space is selected. The Code for Anisotropies in the Microwave Background (Lewis et al. 2000) is used to compute the matter power spectrum at 20 redshift bins between $0 < z < 2.5$, spaced logarithmically in $1 + z$. The matter power spectrum,

cosmological parameters, and Y_{SZ}–M_{500} and Y_X–M_{500} scaling relation parameters are then input to the cluster likelihood function. Y_X is defined as $Y_X \equiv M_g T_X$, where M_g is the cluster gas mass within r_{500}, and T_X is the core-excised X-ray spectroscopic temperature in an annulus between 0.15 and $1.0 \times r_{500}$.

To calculate the cluster likelihood, first the matter power spectrum and cosmological parameters are used to calculate the cluster mass function, based on Tinker et al. (2008). Next, the mass function is converted to the predicted cluster abundance in our observable space, $N(Y_{SZ}, Y_X, z)$. This conversion is accomplished using our standard Y^{θ}_{SZ}–M_{500} scaling relation (Equation (10)), with flat unbounded priors on all parameters, and the Y_X–M_{500} scaling relation from B13:

$$\frac{M_X^{500}}{10^{14} M_\odot\, h^{-1}} = \left(A_X h^{3/2}\right)\left(\frac{Y_X}{3\times 10^{14} M_\odot\,\mathrm{keV}}\right)^{B_X} E(z)^{C_X}, \quad (12)$$

parameterized by the normalization factor A_X, the mass scaling B_X, the redshift evolution C_X, and the log-normal intrinsic scatter D_X. This scaling relation is based on the relation used in Vikhlinin et al. (2009a).

The priors on the Y_X–M_{500} scaling relation parameters were $A_X = 5.77 \pm 0.56$, $B_X = 0.57 \pm 0.03$, $C_X = -0.40 \pm 0.20$, and $D_X = 0.12 \pm 0.08$. All these priors are Gaussian. The slope and normalization priors were motivated by Vikhlinin et al. (2009a), and the priors on the redshift evolution and scatter were motivated by the range observed in several different sets of simulations that included varying astrophysics (Kravtsov et al. 2006; Fabjan et al. 2011). These priors are identical to those used in Benson et al. (2013), and a more detailed description motivating them is given there.

The predicted cluster density as a function of Y_{SZ}, Y_X, and z can be written as follows:

$$\frac{dN(Y_{SZ}, Y_X, z|\boldsymbol{p})}{dY_{SZ}\, dY_X\, dz} = \int P(Y_{SZ}, Y_X|M, z, \boldsymbol{p})\; P(M, z|\boldsymbol{p})\, \Phi(Y_{SZ})\, dM, \quad (13)$$

where $\boldsymbol{p}$ is the set of cosmological and scaling relation parameters, and $\Phi(Y_{SZ})$ is the selection function in Y_{SZ}. This predicted cluster density function differs from B13 in that the selection function must be transformed from a Heaviside step function at $\xi = 5$ into a function of Y_{SZ}. We assume that Y_{SZ} and ξ can be related with a log-normal distributed scaling relation, and that the selection in B13 can therefore be well approximated by an error-function in Y_{SZ}. We then define our selection function as

$$\Phi(Y_{SZ}) = \frac{1}{2}\mathrm{erf}\left(\frac{Y_{SZ} - Y^{\phi}_{SZ}(z)}{\sqrt{2}\, Y^{\phi}_{SZ}(z)\, D}\right) + \frac{1}{2}, \quad (14)$$

where the selection threshold, $Y^{\phi}_{SZ}(z)$ is defined as the Y_{SZ} value corresponding to $\xi = 5$ at the redshift z. We estimate $Y^{\phi}_{SZ}(z)$ by fitting a Y_{SZ}–ξ scaling relation of the form

$$Y_{SZ} = A\xi^B E(z)^C, \quad (15)$$

using the catalog of SPT observed clusters given in R13. The width of the selection error-function is given by the scatter in the Y_{SZ}–ξ scaling relation, D.

We evaluate Equation (13) on a $200 \times 200 \times 30$ grid in (Y_{SZ}, Y_X, z) space, and convolve with a Gaussian error term in Y_{SZ} to account for the measurement noise. The width of the Gaussian is given by the uncertainty in Y_{SZ} as a function of Y_{SZ}, $\delta Y_{SZ}(Y_{SZ})$, as determined by the cluster parameterization MCMC (see Section 5.3).

The likelihood function of the observed cluster sample is defined by the Poisson probability:

$$\log(\mathcal{L}(\boldsymbol{p})) = \sum_i \log\left(\frac{dN(Y_{SZi}, Y_{Xi}, z_i, |\boldsymbol{p})}{dY_{SZ}\, dY_X\, dz}\right) - \int \frac{dN(Y_{SZ}, Y_X, z, |\boldsymbol{p})}{dY_{SZ}\, dY_X\, dz}\, dY_{SZ}\, dY_X\, dz, \quad (16)$$

where the summation is over the SPT clusters in our catalog. Note also that this is the unnormalized log-likelihood.

There is a complication, in that Y_X is dependent on the cosmological parameters. $Y_X \equiv M_g\, T_X$, where M_g is the gas mass within r_{500}, and T_X is the core-excised X-ray temperature in an annulus between $0.15 \times r_{500}$ and $1.0 \times r_{500}$. To maintain consistency with the cosmological parameters, we recalculate Y_X for each cluster at every step in CosmoMC, given the current Y_X–M_{500} relation and r_{500}. In the likelihood, we add $\sum_i \log(Y_{Xi})$ to the right hand side of Equation (16) to account for the recalculation of Y_X. For a detailed explanation of this correction term, see Appendix B of B13.

To account for measurement error in Y_X and z for each cluster, we marginalize over the relevant parameter, weighted by a Gaussian likelihood determined by its uncertainty. For the few clusters without observed Y_X data, we instead weight the marginalized parameter by a uniform distribution over the allowed parameter range.

The likelihood of this set of cosmological and scaling relation parameters is then used by CosmoMC in the acceptance/rejection computation. Only the Y^{θ}_{SZ}–M_{500} scaling relation parameters are of interest to us in this analysis. The cosmological and Y_X–M_{500} scaling relation parameters were used as a cross-check to verify that the results were in agreement with the analysis performed on these clusters in B13, but will not be presented here. All parameters differed from the values presented in B13 by $\ll 1\sigma$.

7.2. Y_{SZ}–M_{500} Scaling Relation Results

We use CosmoMC to fit Y^{θ}_{SZ}–M_{500} scaling relations for a range of angular apertures, and find a broad minimum in scatter in the range 0.′5–0.′75, with a minimum intrinsic log-normal scatter of $21\% \pm 11\%$. For these scaling relation parameters we apply flat, unbounded priors. The scatter in the ζ–M_{500} scaling relation for these clusters is comparable, at $21\% \pm 9\%$. The scaling relation parameters for the $Y^{0.'75}_{SZ}$–M_{500} scaling relation are given in Table 1.

We also fit mass scaling relations for Y^{ρ}_{SZ} integrated within a range of physical radii, ρ, from 0.1 Mpc to 0.5 Mpc. We find a broad minimum in scatter in the range 0.2–0.3 Mpc, with a minimum intrinsic log-normal scatter of $23\% \pm 5\%$. This is comparable to the scatter in both the ζ and $Y^{0.'75}_{SZ}$ mass scaling relations. The parameters for the nominal $Y^{0.3\,\mathrm{Mpc}}_{SZ}$ mass scaling relation (0.3 Mpc corresponds to 0.′75 at the survey median redshift of $z = 0.6$) are listed in Table 1.

7.3. Cluster Masses

To calculate the masses of the clusters, the $Y^{0.'75}_{SZ}$ CosmoMC chains were used. The probability density function for the mass

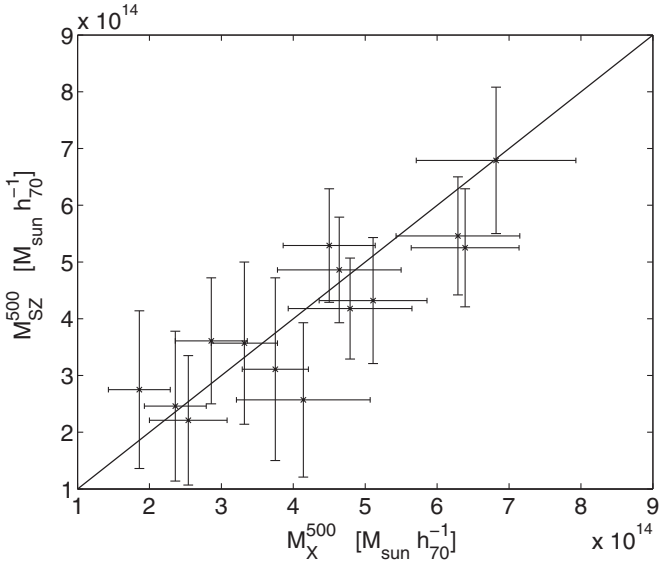

Figure 8. Masses computed from $Y_{SZ}^{0.'75}$ for the 14 SPT observed clusters in Table 2 with follow-up X-ray observations vs. corresponding M_X^{500} values. For reference we overplot the relation $M_{SZ}^{500} = M_X^{500}$.

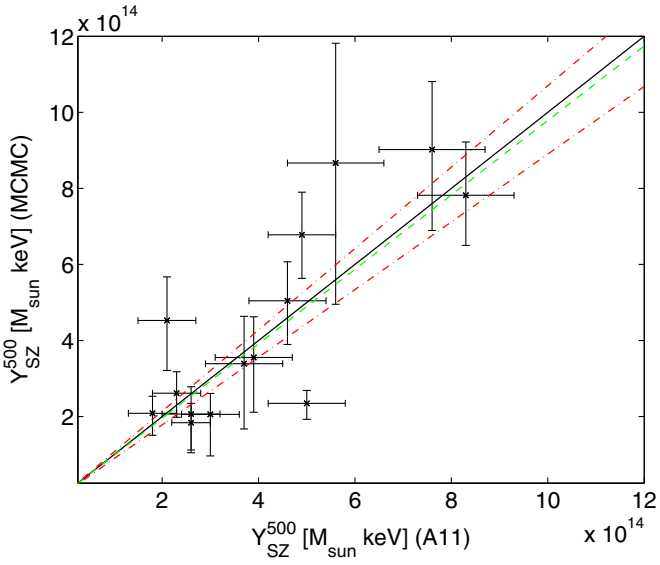

Figure 9. Y_{SZ}^{500} for the 14 SPT clusters from Table 2 with follow-up X-ray observations, calculated by the MCMC method described here, and by the MF method of Andersson et al. (2011). We also show the reference line $Y_{SZ}^{500}(\mathrm{MCMC}) = Y_{SZ}^{500}(\mathrm{A11})$ (solid), the best-fit line (green dashed), and the uncertainty in the fit defined as the range for which $\Delta\chi^2 < 1$ compared to the best fit (red dot-dashed). The best-fit normalization is $A = 0.98 \pm 0.09$, demonstrating that the scaling relation is consistent with equality between $Y_{SZ}^{500}(\mathrm{MCMC})$ and $Y_{SZ}^{500}(\mathrm{A11})$.

was computed on an evenly spaced mass grid for each step in the CosmoMC chains. These probability density functions were then summed to obtain a mass estimate fully marginalized over all scaling relation and cosmological parameters. This was done for CosmoMC chains containing only $Y_{SZ}^{0.'75}$ data, and no Y_X data, and vice versa, to obtain mass estimates based on only the SZ and X-ray data, respectively. The cluster M_{500} masses derived from the $Y_{SZ}^{0.'75}$ and Y_X data (M_{SZ}^{500} and M_X^{500}, respectively) can be found in Table 2, along with the corresponding $Y_{SZ}^{0.'75}$ and Y_X values. $Y_{SZ}^{0.'75}$ values are given in $M_\odot$ keV for ease of comparison with Y_X.

Figure 8 shows the cluster masses calculated from the Y_{SZ}–M_{500} scaling relation versus the masses calculated from the Y_X–M_{500} scaling relation for the B13 cluster sample. The solid line is the reference line $M_{SZ}^{500} = M_X^{500}$.

7.4. $Y_{SZ}(r_{500})$

The self-similar model of cluster formation assumes that clusters scale in well-defined ways based on their mass, typically defined within physical radii proportional to the critical density of the universe at the cluster's redshift (e.g., Kravtsov & Borgani 2012; Kaiser 1984). For this reason, studies of the scaling relations of clusters typically measure physical observables defined by this physical radius, usually r_{500}. In this section we will calculate $Y_{SZ}(r_{500})$, denoted Y_{SZ}^{500}, for comparison with other published parameters for the clusters in B13.

We investigated a method for estimating r_{500} from SZ data, as a way to measure Y_{SZ}^{500} solely from SZ data. This method proved to be problematic, however, because it required estimating M_{500} from a fixed angular aperture, and calculating r_{500} from that estimate. This results in the scatter in the $Y_{SZ}^{0.'75}$–M_{500} scaling relation feeding back into the calculation of Y_{SZ}^{500}. Instead, we use the X-ray determined r_{500} in our calculations of Y_{SZ}^{500}.

In Table 2, we give the measured Y_{SZ}^{500} values for our cluster sample. We note that, as defined in Equation (7), the MCMC fits for a cylindrically projected measure of Y_{SZ}^{500} rather than the spherical de-projected value often used in other Y_{SZ}–M scaling relation results (e.g., A11; Arnaud et al. 2010). Y_{SZ}^{500} values are given in $M_\odot$ keV here, for comparison with A11.

A11 describe a template fitting method of estimating Y_{SZ}^{500}, which uses an SZ source template motivated from X-ray measurements of each cluster. The profile is assumed to match the product of the best-fit gas density profile to the X-ray measurements of each cluster, and the universal temperature profile of Vikhlinin et al. (2006). These profiles are multiplied together to produce the radial pressure profile, and projected onto the sky using a line-of-sight integral through the cluster. A11 then construct a spatial filter using Equation (1), and this X-ray derived source model. The X-ray determined cluster position is used to place priors on the cluster location to prevent maximization bias in the recovered Y_{SZ}^{500} values. Y_{SZ}^{500} is calculated by integrating the source model over a solid angle corresponding to r_{500}, as in Equation (7).

In Figure 9, we plot the Y_{SZ}^{500} estimated by the MCMC method against the Y_{SZ}^{500} estimated by the template fitting method in A11. The best fit relation between the two is $Y_{SZ}^{500}(\mathrm{MCMC}) = (0.98 \pm 0.09)\, Y_{SZ}^{500}(\mathrm{A11})$, where the uncertainty is the range for which $\Delta\chi^2 < 1$ (68% confidence limit) compared to the best-fit. (For a treatment of the calculation of χ^2 with uncertainty in both variables, see, for example, Numerical Recipes in C++, Section 15.3, Press et al. 2002.) We see that these two methods of calculating Y_{SZ}^{500} are consistent, that is, the best-fit scaling relation is consistent with equality between $Y_{SZ}^{500}(\mathrm{MCMC})$ and $Y_{SZ}^{500}(\mathrm{A11})$. The scatter about the expected one-to-one line here is dominated by differences in cluster model shape between the two methods (X-ray derived SZ profile versus β-model).

We also verify that our Y_{SZ}^{500} values for these clusters are in agreement with the Y_X values presented in B13, given the expected Y_{SZ}–Y_X scaling. Figure 10 shows the Y_{SZ}^{500} values of

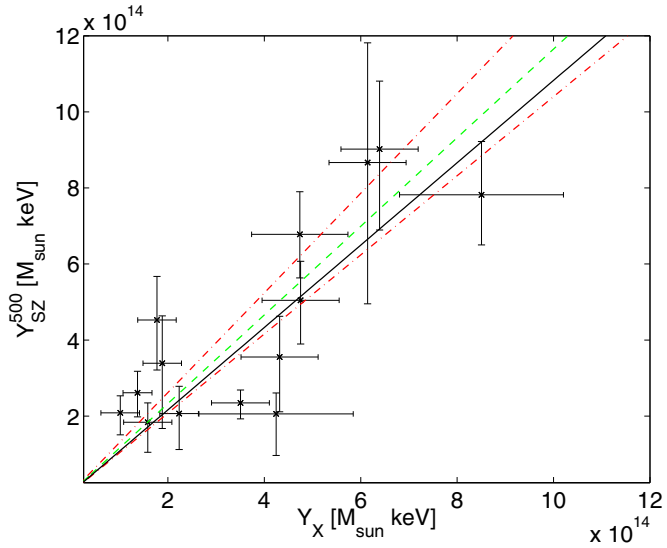

Figure 10. Y_{SZ}^{500}(MCMC) vs. Y_X for the 14 SPT clusters from Table 2 with follow-up X-ray observations. We also show the expected scaling relation from Arnaud et al. (2010): $Y_{SZ}^{500} = 1.08\ Y_X$ (solid), the best-fit line (green dashed), and the uncertainty in the fit defined as the range for which $\Delta\chi^2 < 1$ compared to the best fit (red dot-dashed). The best-fit normalization is $A = 1.17 \pm 0.12$, consistent with the expected scaling between Y_{SZ}^{500} and Y_X.

our catalog of SPT observed clusters plotted against their Y_X values from B13.

We can make a prediction of the relationship between Y_{SZ} and Y_X based on the universal pressure profile from Arnaud et al. (2010), based on X-ray measurements of a representative sample of local, massive clusters. Even though Y_{SZ} and Y_X are effectively measures of the cluster pressure, they depend on the details of the shape of the profile differently, which can still vary somewhat between clusters. Assuming the Arnaud et al. (2010) pressure profile, we predict a relationship of $Y_{SZ}^{500} = 1.08\ Y_X$, where Y_{SZ}^{500} is integrated within a fixed angular aperture corresponding to r_{500} (often called a cylindrical projection). In Figure 10, we plot the Y_{SZ} estimated by the MCMC method against the Y_X measured in B13. We fit a scaling relation of the form $Y_{SZ}^{500} = A\ Y_X$, and find that the best-fit normalization is $A = 1.17 \pm 0.12$, consistent with the expected normalization. This fit has a total χ^2 of 19.46 for 14 degrees of freedom, with a probability to exceed of $P = 0.15$. The uncertainty in the normalization is the range for which $\Delta\chi^2 < 1$ compared to the best fit.

8. CONCLUSIONS

We describe and implement a method of constraining Y_{SZ} generalizable to any cluster profile, and we show that this method accurately recovers Y_{SZ} in simulations. We compare Y_{SZ} to SPT cluster detection significance, focusing on scatter with mass. Finally, we apply this method to clusters detected in the SPT-SZ survey, and compare the estimated Y_{SZ} values to Y_{SZ} estimated by a template fitting method, and to Y_X.

We apply our method to clusters in simulated tSZ-only maps and measure Y_{SZ}^{θ}, the integrated Comptonization within a constant angular aperture. We find that Y_{SZ} is measured with the lowest fractional scatter in an aperture comparable to the SPT beam size ($\sim 1'$ FWHM at 150 GHz). We fit Y_{SZ}^{θ}–M_{vir} scaling relations for a range of angular apertures and find a minimum fractional scatter of 23% ± 2% in Y_{SZ}, at a fixed mass, with the minimum occurring for an angular aperture of 0.′75. We also calculate Y_{SZ} within a range of physical radii, ρ, and find a minimum scatter in Y_{SZ}^{ρ} at an integration radius of 0.3 Mpc, which corresponds roughly to 0.′75 at the survey median redshift ($z = 0.6$), with a fractional scatter of 28% ± 2% at a fixed mass. Using the same simulated clusters, we also fit a ζ–M_{vir} relation, where ζ is the MF SZ detection significance measured by SPT, and find a fractional scatter of 27% ± 2%.

We also analyze clusters in simulations including tSZ, CMB, point sources, atmospheric noise, and realistic SPT instrumental noise. In these full-noise simulations, the $Y_{SZ}^{0.'75}$–M_{vir} scaling relation has 27% ± 1% scatter, the $Y_{SZ}^{0.3\ Mpc}$–M_{vir} scaling relation has 34% ± 2% scatter, and ζ–M_{vir} scaling relation has 27% ± 2 % scatter. These simulations demonstrate that scatter in Y_{SZ}^{θ} is comparable to the scatter in ζ.

To investigate Y_{SZ} scaling relations in SPT observed clusters, we fit Y_{SZ}^{θ}–M_{500} and Y_{SZ}^{ρ}–M_{500} scaling relations to the sample of 18 SPT clusters described and examined in Benson et al. (2013). Of these, 14 have X-ray observations and measured Y_X values, which we use to estimate the cluster M_{500} masses. We fit the scaling relations using a version of CosmoMC, similar to the one described in Benson et al. (2013), modified to account for the cluster selection based on Y_{SZ} instead of SPT significance. For these clusters, the $Y_{SZ}^{0.'75}$–M_{500} scaling relation is found to have 21% ± 11% intrinsic log-normal scatter in Y_{SZ} at a fixed mass, the $Y_{SZ}^{0.3\ Mpc}$–M_{500} scaling relation has 26% ± 9% scatter, and the ζ–M_{500} relation has 21% ± 9% scatter.

We also calculate a cylindrically projected Y_{SZ}^{500}, the integrated Comptonization within r_{500}, for the clusters in the Benson et al. (2013) sample. We compare the Y_{SZ}^{500} values recovered by our Markov Chain Monte Carlo method to those calculated for the same clusters by the template fitting method described in A11 and find the two methods to be consistent. We further compare the MCMC derived Y_{SZ}^{500} values to the Y_X values for these clusters from Benson et al. (2013) and find that they are consistent with the expected scaling between Y_{SZ} and Y_X, based on the universal pressure profile of Arnaud et al. (2010).

We have demonstrated, with both simulations with realistic SPT noise and SPT observed clusters, that Y_{SZ} is most accurately determined in an aperture comparable to the SPT beam size. We have used this information in measuring Y_{SZ} for the catalog of clusters observed with the SPT in the 2008 and 2009 seasons (Reichardt et al. 2013). The SPT-SZ survey of 2500 deg^2 was completed in 2011 November, and has detected ∼500 clusters with a median redshift of ∼0.5 and a median mass of $M_{500} \sim 2.3 \times 10^{14} M_{\odot}\, h^{-1}$. The methods and results presented here will inform the measurement and use of Y_{SZ} for the clusters detected in the full SPT-SZ survey.

The South Pole Telescope program is supported by the National Science Foundation through grant ANT-0638937. Partial support is also provided by the NSF Physics Frontier Center grant PHY-0114422 to the Kavli Institute of Cosmological Physics at the University of Chicago, the Kavli Foundation, and the Gordon and Betty Moore Foundation.

We acknowledge the use of the Legacy Archive for Microwave Background Data Analysis (LAMBDA). Support for LAMBDA is provided by the NASA Office of Space Science. Galaxy cluster research at Harvard is supported by NSF grant AST-1009012. Galaxy cluster research at SAO is supported in part by NSF grants AST-1009649 and MRI-0723073. The McGill group acknowledges funding from the National Sciences and Engineering Research Council of Canada, Canada Research

Chairs program, and the Canadian Institute for Advanced Research. The Munich group was supported by The Cluster of Excellence "Origin and Structure of the Universe," funded by the Excellence Initiative of the Federal Government of Germany, EXC project number 153. R.J.F. is supported by a Clay Fellowship, and B.A.B. is supported by a KICP Fellowship. A.P. is supported by an NSF Graduate Research Fellowship under grant No. DGE-1144152. J.H.L. is supported by NASA through the Einstein Fellowship Program under grant No. PF2-130094. M.M. acknowledges support provided by NASA through a Hubble Fellowship grant from STScI. M.D. acknowledges support from an Alfred P. Sloan Research Fellowship, W.F. and C.J. acknowledge support from the Smithsonian Institution, and B.S. acknowledges support from the Brinson Foundation.

Facilities: Blanco (MOSAIC), *CXO* (ACIS), Gemini-South (GMOS), Magellan:Baade (IMACS), Magellan:Clay (LDSS3), SPT, *XMM* (EPIC)

REFERENCES

AMI Consortium Olamaie, M., Rodríguez-González, C., et al. 2012a, MNRAS, 421, 1136
AMI Consortium, Rodríguez-González, C., Shimwell, T. W., et al. 2012b, MNRAS, 425, 162
Andersson, K., Benson, B. A., Ade, P. A. R., et al. 2011, ApJ, 738, 48
Arnaud, M., Pratt, G. W., Piffaretti, R., et al. 2010, A&A, 517, A92
Barbosa, D., Bartlett, J., Blanchard, A., & Oukbir, J. 1996, A&A, 314, 13
Benson, B. A., Church, S. E., Ade, P. A. R., et al. 2004, ApJ, 617, 829
Benson, B. A., de Haan, T., Dudley, J. P., et al. 2013, ApJ, 763, 147
Bertin, E., & Arnouts, S. 1996, A&AS, 117, 393
Bode, P., Ostriker, J. P., Weller, J., & Shaw, L. 2007, ApJ, 663, 139
Bonamente, M., Joy, M. K., Carlstrom, J. E., Reese, E. D., & LaRoque, S. J. 2004, ApJ, 614, 56
Bonamente, M., Joy, M. K., LaRoque, S. J., et al. 2006, ApJ, 647, 25
Brodwin, M., Ruel, J., Ade, P. A. R., et al. 2010, ApJ, 721, 90
Carlstrom, J. E., Ade, P. A. R., Aird, K. A., et al. 2011, PASP, 123, 568
Carlstrom, J. E., Holder, G. P., & Reese, E. D. 2002, ARA&A, 40, 643
Cavaliere, A., & Fusco-Femiano, R. 1976, A&A, 49, 137
Culverhouse, T. L., Bonamente, M., Bulbul, E., et al. 2010, ApJL, 723, L78
De Zotti, G., Ricci, R., Mesa, D., et al. 2005, A&A, 431, 893
Desai, S., Armstrong, R., Mohr, J. J., et al. 2012, ApJ, 757, 83
Dunkley, J., Komatsu, E., Nolta, M. R., et al. 2009, ApJS, 180, 306
Fabjan, D., Borgani, S., Rasia, E., et al. 2011, MNRAS, 416, 801
Granato, G. L., De Zotti, G., Silva, L., Bressan, A., & Danese, L. 2004, ApJ, 600, 580
Haehnelt, M. G., & Tegmark, M. 1996, MNRAS, 279, 545
Halverson, N. W., Lanting, T., Ade, P. A. R., et al. 2009, ApJ, 701, 42
Hasselfield, M., Hilton, M., Marriage, T. A., et al. 2013, JCAP, 7, 8
Hastings, W. K. 1970, Biometrika, 57, 97
Herranz, D., Sanz, J. L., Barreiro, R. B., & Martínez-González, E. 2002a, ApJ, 580, 610
Herranz, D., Sanz, J. L., Hobson, M. P., et al. 2002b, MNRAS, 336, 1057
High, F. W., Stalder, B., Song, J., et al. 2010, ApJ, 723, 1736
Hobson, M. P., & McLachlan, C. 2003, MNRAS, 338, 765
Holder, G. P., & Carlstrom, J. E. 2001, ApJ, 558, 515
Itoh, N., Kohyama, Y., & Nozawa, S. 1998, ApJ, 502, 7
Kaiser, N. 1984, ApJL, 284, L9
Kravtsov, A. V., & Borgani, S. 2012, ARA&A, 50, 353
Kravtsov, A. V., Vikhlinin, A., & Nagai, D. 2006, ApJ, 650, 128
LaRoque, S. J., Bonamente, M., Carlstrom, J. E., et al. 2006, ApJ, 652, 917
Lewis, A., & Bridle, S. 2002, PhRvD, 66, 103511
Lewis, A., Challinor, A., & Lasenby, A. 2000, ApJ, 538, 473
Lueker, M., Reichardt, C. L., Schaffer, K. K., et al. 2010, ApJ, 719, 1045
Mantz, A., Allen, S. W., Ebeling, H., Rapetti, D., & Drlica-Wagner, A. 2010, MNRAS, 406, 1773
Marriage, T. A., Baptiste Juin, J., Lin, Y.-T., et al. 2011, ApJ, 731, 100
Marrone, D. P., Smith, G. P., Okabe, N., et al. 2012, ApJ, 754, 119
Marrone, D. P., Smith, G. P., Richard, J., et al. 2009, ApJL, 701, L114
Marsden, D., Gralla, M., Marriage, T. A., et al. 2013, MNRAS, 439, 1556
Melin, J.-B., Bartlett, J. G., & Delabrouille, J. 2006, A&A, 459, 341
Metropolis, N., Rosenbluth, A. W., Rosenbluth, M. N., Teller, A. H., & E. Teller 1953, JChPh, 21, 1087
Mocanu, L. M., Crawford, T. M., Vieira, J. D., et al. 2013, ApJ, 779, 61
Motl, P. M., Hallman, E. J., Burns, J. O., & Norman, M. L. 2005, ApJL, 623, L63
Muchovej, S., Mroczkowski, T., Carlstrom, J. E., et al. 2007, ApJ, 663, 708
Nagai, D., Kravtsov, A. V., & Vikhlinin, A. 2007, ApJ, 668, 1
Negrello, M., Perrotta, F., González-Nuevo, J., et al. 2007, MNRAS, 377, 1557
Nozawa, S., Itoh, N., Kawana, Y., & Kohyama, Y. 2000, ApJ, 536, 31
Planck and AMI Collaborations, Ade, P. A. R., Aghanim, N., et al. 2013, A&A, 550, A128
Planck Collaboration, Ade, P. A. R., Aghanim, N., et al. 2011a, A&A, 536, A8
Planck Collaboration, Ade, P. A. R., Aghanim, N., et al. 2012, A&A, 550, A131
Planck Collaboration, Ade, P. A. R., Aghanim, N., et al. 2013a, A&A, 571, A29
Planck Collaboration, Ade, P. A. R., Aghanim, N., et al. 2013b, A&A, 571, A20
Planck Collaboration, Aghanim, N., Arnaud, M., et al. 2011b, A&A, 536, A10
Press, W. H., Teukolsky, S. A., Vetterling, W. T., & Flannery, B. P. 2002, Numerical Recipes in C++: The Art of Scientific Computing (Cambridge: Cambridge Univ. Press)
Reese, E. D., Mroczowski, T., Menanteau, F., et al. 2012, ApJ, 751, 12
Reichardt, C. L., Stalder, B., Bleem, L. E., et al. 2013, ApJ, 763, 127
Rozo, E., Wechsler, R. H., Rykoff, E. S., et al. 2010, ApJ, 708, 645
Ruel, J., Bazin, G., Bayliss, M., et al. 2013, ApJ, 792, 45
Sayers, J., Czakon, N. G., Mantz, A., et al. 2013, ApJ, 768, 177
Schaffer, K. K., Crawford, T. M., Aird, K. A., et al. 2011, ApJ, 743, 90
Sehgal, N., Trac, H., Acquaviva, V., et al. 2011, ApJ, 732, 44
Shaw, L. D., Nagai, D., Bhattacharya, S., & Lau, E. T. 2010, ApJ, 725, 1452
Sifon, C., Menanteau, F., Hasselfield, M., et al. 2013, ApJ, 772, 25
Staniszewski, Z., Ade, P. A. R., Aird, K. A., et al. 2009, ApJ, 701, 32
Sunyaev, R. A., & Zel'dovich, Y. B. 1972, CoASP, 4, 173
Tinker, J., Kravtsov, A. V., Klypin, A., et al. 2008, ApJ, 688, 709
Vanderlinde, K., Crawford, T. M., de Haan, T., et al. 2010, ApJ, 722, 1180
Vieira, J. D., Crawford, T. M., Switzer, E. R., et al. 2010, ApJ, 719, 763
Vikhlinin, A., Burenin, R. A., Ebeling, H., et al. 2009a, ApJ, 692, 1033
Vikhlinin, A., Kravtsov, A. V., Burenin, R. A., et al. 2009b, ApJ, 692, 1060
Vikhlinin, A., Kravtsov, A., Forman, W., et al. 2006, ApJ, 640, 691
Williamson, R., Benson, B. A., High, F. W., et al. 2011, ApJ, 738, 139